

Super4DR: 4D Radar-centric Self-supervised Odometry and Gaussian-based Map Optimization

Zhiheng Li, Weihua Wang, Qiang Shen, Yichen Zhao, and Zheng Fang*

Abstract—Conventional SLAM systems using visual or LiDAR data often struggle in poor lighting and severe weather. Although 4D radar is suited for such environments, its sparse and noisy point clouds hinder accurate odometry estimation, while the radar maps suffer from obscure and incomplete structures. Thus, we propose Super4DR, a 4D radar-centric framework for learning-based odometry estimation and gaussian-based map optimization. First, we design a cluster-aware odometry network that incorporates object-level cues from the clustered radar points for inter-frame matching, alongside a hierarchical self-supervision mechanism to overcome outliers through spatio-temporal consistency, knowledge transfer, and feature contrast. Second, we propose using 3D gaussians as an intermediate representation, coupled with a radar-specific growth strategy, selective separation, and multi-view regularization, to recover blurry map areas and those undetected based on image texture. Experiments show that Super4DR achieves a 67% performance gain over prior self-supervised methods, nearly matches supervised odometry, and narrows the map quality disparity with LiDAR while enabling multi-modal image rendering.

Index Terms—4D radar, Self-supervised odometry estimation, Gaussian splatting, Simultaneous localization and mapping.

I. INTRODUCTION

SIMULTANEOUS localization and mapping is essential for autonomous robots. Over the past decade, LiDAR and visual SLAM have achieved significant progress, enabling real-time operation with high precision in favorable environments. However, LiDAR is susceptible to atmospheric scattering and particulate matter in inclement weather, causing degraded data integrity or a complete loss of functionality. Similarly, cameras become ineffective in poor illumination or dense smoke. These limitations pose fundamental challenges to reliable localization and scene reconstruction in such adverse situations.

Fortunately, 4D radar has emerged as a promising solution to these issues. Its longer wavelengths provide superior signal penetration and all-weather robustness compared with LiDAR. Additionally, unlike high-cost scanning radar limited to coarse planar imaging and 3D single-chip automotive radar with low resolution, 4D radar provides point cloud data that can describe the approximate contour of objects. Consequently, recent studies have developed geometric and end-to-end frameworks for 4D radar odometry, aiming for reliable pose estimation in challenging weather. However, geometry-based algorithms [1]–[4] that rely on dense and precise structural association encounter limitations due to the characteristics of radar points (Fig. 1(a)).

- 1) *Limited geometric primitives*: The sparser radar data lacks distinct geometric elements (e.g., lines and planes), which act as essential constraints for traditional registration approaches.
- 2) *Measurement uncertainty*: More severe positional noise in range and azimuth violates the rigid geometric assumptions

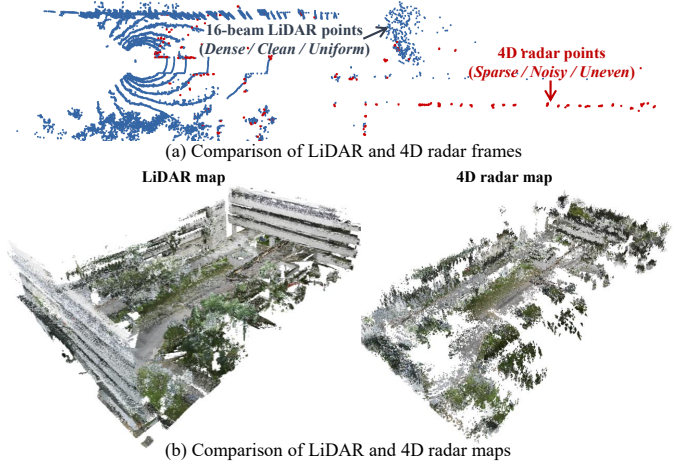


Fig. 1. Comparison of LiDAR and 4D radar data. Unlike LiDAR, 4D radar points usually suffer from greater sparsity, noise, and uneven density, thereby posing challenges for robust odometry estimation and high-integrity mapping. Here, the maps are constructed based on ground-truth poses provided by the NTU4DRadLM [9] dataset.

of conventional methods. In comparison, learning-based methods [5]–[8] are capable of extracting information-rich features from low-quality radar points. They further model inter-frame relationships using adaptive matching within high-dimensional feature space to alleviate the impact of noise, thereby pushing the boundaries of 4D radar odometry.

However, supervised learning depends on expensive ground truths that are difficult to obtain in harsh conditions. Although self-supervised algorithms [7], [8] are label-free, their accuracy lags notably behind supervised approaches due to over-reliance on rigid geometric constraints that are easily disrupted by radar noise and measurement errors. Meanwhile, they inherit point-level matching originally designed for uniform LiDAR points, which may be suboptimal for the blocky distribution of radar points and fail to exploit latent object cues. Beyond odometry, the maps built from 4D radar points are too loose and indistinct (Fig. 1(b)). While utilizing diffusion networks [10], [11] is a way for point cloud completion, they struggle to reconstruct objects outside radar's field of view (e.g., inferring a complete tree from a single trunk without rich geometric priors) and face a critical bottleneck in scene generalization. Furthermore, most existing works focus on enhancing radar frames independently, leaving the optimization of the entire map as a challenging and open topic. Thus, in this article, we propose a 4D radar-centric framework called *Super4DR*, as illustrated in Fig. 2, to address the radar limitations in accurate pose estimation and complete map reconstruction.

For radar odometry, building upon radar properties, we propose a cluster-aware network with multi-level self-supervision,

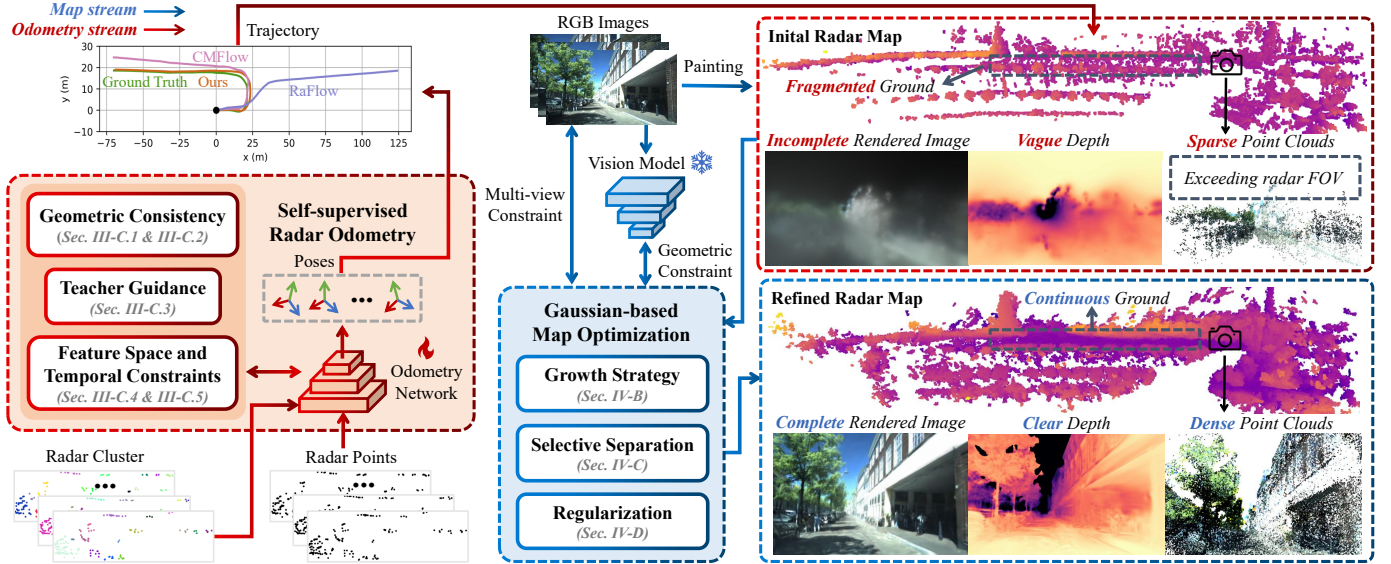


Fig. 2. Overview of Super4DR framework with end-to-end radar odometry and gaussian-based map optimization. First, a cluster-aware network, trained with multi-level self-supervised losses, processes radar points along with cluster grouping to estimate poses. Afterwards, an initial map with incomplete structures is constructed based on the trajectory and painted through image pixels. We further propose a map optimizer adopting gaussians as an intermediate representation, with a radar-specific growth strategy, selective separation and multi-view regularization for complete map reconstruction and detailed image rendering.

moving beyond sole reliance on geometric constraints. Specifically, we use clustering information derived from point distribution to enable the network to learn inter-frame relationships at the object level while suppressing the point-level noise. We further introduce a *cluster-weighted distance* loss to supervise geometric alignment, with particular emphasis on large, stable point clusters. Next, we present a *column occupancy* loss that represents points as grid occupation, allowing for tolerance of noisy positions and ensuring large-scale consistency through column-wise similarity. Beyond rigid spatial consistency rules, a geometry-based approach serves as a *teacher* to produce soft pose labels based on a secondary refinement and selection mechanism, distilling meaningful knowledge into the network. Additionally, we adopt a *feature contrast* loss to maximize the feature difference of non-corresponding point pairs for reliable matching and design a constant-acceleration *motion model* for trajectory smoothing.

For map optimization, encouraged by 3D gaussian splatting (3DGS [12]), we believe that converting the 4D radar map into gaussian representation and optimizing it could enhance map quality, grounded in several capabilities of 3DGS framework. **First**, benefiting from splitting and cloning mechanisms, radar gaussians can multiply adaptively based on gradients to occupy structural voids, while their positions are adjusted to generate dense geometry under image supervision. **Second**, because of the image's larger vertical FOV, gaussians are forced to expand and recover undetected regions of radar to guarantee that their rendered output aligns with image pixels correctly, thereby improving map integrity. **Third**, with the help of cross-modal and full-map optimization without neural network, it can avoid generalization problems and ensure greater global consistency than frame-wise point refinement. Once optimization finishes, refined gaussians can be reverted into points according to their centroids, producing a complete and structurally coherent map.

Nevertheless, directly using 3DGS [12] is “insufficient” as it prioritizes rendering quality over geometric accuracy, while

gaussians initialized from radar maps with uneven point distribution and noise cause challenges for subsequent optimization. Thus, we propose a *growth strategy* that first creates synthetic gaussians using depth priors derived from a visual fundamental model to solve the ground fragmentation issue unique to radar maps. Unlike the densification manner that only meets image rendering requirements in most GS-based methods, we adopt a geometric-aware strategy that splits and interpolates gaussians based on local geometry to generate denser structures. Besides, *selective separation* decouples sky gaussians by maintaining a mask to decrease floaters and saves valuable large gaussians from periodic pruning for subsequent completion. Rather than optimizing gaussians based on a single view with ambiguous spatial information one by one, we introduce a *multi-view regularization* that leverages overlapping regions to jointly refine noisy radar gaussians into deterministic states. Furthermore, geometric priors from visual foundation models are utilized as extra supervision to improve the geometric accuracy of maps.

In summary, the contributions of this paper are as follows:

- To the best of our knowledge, Super4DR is the first integrated framework that considers both radar odometry and map optimization, empowering pose prediction from low-quality radar points and reconstruction of clear structures from initially indistinct maps.
- We propose a cluster-aware odometry network trained by a multi-level self-supervision strategy, including cluster-weighted distance, column occupancy, teacher guidance, and the constraints on feature-space and temporal aspects, to mitigate the impact of outliers on the learning process.
- We innovatively employ 3D gaussian representation as an intermediary to enhance map quality, developing gaussian growth strategy with depth-guided ground completion and geometry-aware densification, complemented by selective separation and multi-view overlap regularization, thereby recovering blurry structures and radar-undetected areas.
- Experiments on public and self-collected datasets indicate

that our radar odometry achieves state-of-the-art results among self-supervised algorithms while remarkably closing the gap to recent supervised methods. Super4DR also exceeds previous GS-based works in radar map and rendered image quality, validating that gaussian splatting can be a viable new approach for 4D radar map optimization.

- We additionally explore the potential of 4D radar-thermal gaussian splatting in low-light conditions and demonstrate the applicability of our algorithm across different visual sensors, including both RGB and thermal cameras. Our code and multi-sensor dataset based on a handheld platform will be released in <https://github.com/NEU-REAL/Super4DR> to promote the development of related fields.

II. RELATED WORK

A. LiDAR-based Odometry

The purpose of odometry is to calculate pose transformation between adjacent frames. As a pioneering method, the iterative closest point (ICP) [13] is widely adopted for point cloud registration by minimizing point-to-point distance, but it exhibits sensitivity to noise. Its variants, like point-to-line and point-to-plane ICP, exploit local geometry to enhance robustness, while GICP [14] merges their advantages. KISS-ICP [15] unleashes the potential of point-to-point matching by employing adaptive thresholds for data association and outlier rejection. NDT [16] forms a voxel-based probability distribution from point clouds, bypassing point correspondences. For efficiency, LOAM [17] extracts edge and plane features to perform matching. Building on it, Lego-LOAM [18] incorporates ground segmentation for noise filtering, then F-LOAM [19] reduces computation burden through non-iterative two-step compensation.

With the rise of deep learning, many studies are dedicated to end-to-end odometry methods, achieving competitive results. PWCL-Net [20] and EfficientLO [21] introduce a coarse-to-fine framework to iteratively match point clouds and leverage masks to suppress the effect of dynamic objects. TransLO [22] employs window-based attention to extract global features for reliable registration, and DSLO [23] utilizes historical features as hidden states to raise prediction continuity. While effective, these supervised learning methods require costly labels. Thus, DeLORA [24] uses a KD-Tree to search for target pairs based on predicted pose and adopts point-to-plane and plane-to-plane error metrics to optimize model. HPPLO-Net [25] then boosts network robustness using hierarchical point-to-plane distances as supervision. RSLLO [26] partitions point clouds into multiple sub-regions, estimates ego-motion by regional voting, and uses uncertainty-aware geometric loss for self-supervised training. Although these LiDAR-based algorithms work well in normal conditions, their performance markedly drops with point cloud degradation from smoke and adverse weather.

B. Radar-based Odometry

To achieve odometry estimation in challenging scenes, early works utilize scanning radar as the primary sensor, employing point-to-line metric minimization [27], feature point extraction and matching [28] or improved NDT with the outlier filter [29] to estimate ego-motion. However, the blurred 2D imaging of

the sensor limits odometry precision and map quality. Its large volume and high cost also hinder the practical application. By contrast, compact, low-cost and higher-precision 4D radar has attracted research attention. As an initial study, APDGICP [1] extends GICP with probabilistic distributions to improve scan matching. EFEAR-4D [2] applies a scan-to-map mechanism to form denser spatial correspondences for pose solving. Besides, a doppler-based ICP [3] is presented to harness radar velocity information, and RCS-weighted registration [4] is proposed to handle inherent sparsity and measurement noise in radar data.

Recently, end-to-end methods have demonstrated strong performance. For example, 4DRONet [5] separately encodes radar information with different properties and constructs two-stage pose refinement. CMFlow [30] leverages cross-modal supervision from multi-sensor data to jointly train a network for scene flow and ego-motion estimation. Then, CAO-RONet [31] uses local completion to supply denser constraints for matching and adopts multi-level resilient registration with feature similarity to suppress noise influence. Besides, 4DRV-Net [6] presents a multi-modal method that integrates rich image information to assist sparse point matching. To remove reliance on labels, RaFlow [8] computes relative poses from predicted scene flow, subsequently optimizing the model based on chamfer distance. SelfFRO [7] further applies spherical reprojection and velocity-aware loss to achieve notable improvement, but there is still a significant gap against supervised methods. More importantly, most methods focus on the pose accuracy but neglect the map quality. Thus, the constructed radar map remains noisy, vague and incomplete as a result of the low-quality 4D radar points.

C. 3D Gaussian Splatting

Unlike Neural Radiance Fields (NeRFs) [32] that use MLP to learn implicit neural scenes, 3DGS [12] represents scenarios as explicit gaussian ellipsoids whose parameters are optimized by differentiable rasterization and image reconstruction losses, enabling faster convergence and rendering speed. On this basis, GaussianPro [33] proposes a propagation operation to generate reliable rendered depths and normals, which are further applied to yield new gaussians to populate under-reconstructed regions and enhance image details. To promote geometric optimization in sparse views, DNGaussian [34] presents hard and soft depth regularization to drive the movement of gaussians and reshape space structure. As 3DGS struggles with precise surface fitting, 2DGS [35] proposes planar 2D gaussians with view-consistent geometry to exactly model thin surfaces. To reconstruct scenes at real scale, some works [36]–[38] integrate LiDAR points to initialize gaussians. LiV-GS [36] uses a conditional constraint to guide gaussian optimization in areas lacking LiDAR depth. HGS-Mapping [37] optimizes hybrid gaussians with different classes, while DrivingGaussian [38] represents dynamic scenes by decoupling gaussians for static and moving objects.

Although advances have been made in LiDAR-based scene reconstruction [36]–[38] and map post-processing [39], [40], little attention has been paid to enhancing 4D radar maps, overlooking their potential for mapping under adverse conditions. Moreover, no existing studies have explored gaussian splitting for optimizing maps built by 4D radar. This is a distinct topic

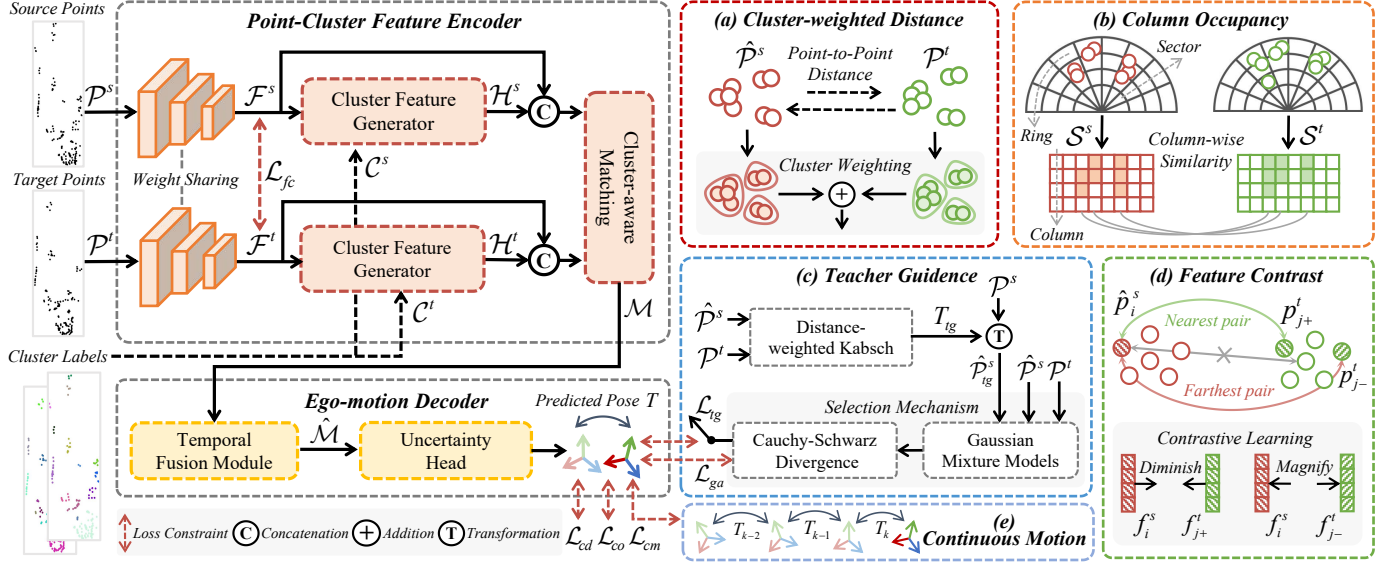


Fig. 3. Framework of end-to-end radar odometry with multi-level constraints. The odometry network consists of a point-cluster feature encoder and an ego-motion decoder. For self-supervised training, the loss functions first include cluster-weighted distance and column-wise occupancy comparison, which account for the distribution and noise properties of radar points. Network learning is further selectively guided via soft labels generated by a geometry-based algorithm. We also facilitate discriminative feature extraction using feature contrast, while enforcing motion smoothness through a constant-acceleration assumption.

because the sparsity and non-uniformity of radar points, unlike LiDAR data, leave numerous spatial positions uninitialized and hinder later optimization due to missing geometric priors.

III. SELF-SUPERVISED RADAR ODOMETRY WITH MULTI-LEVEL CONSTRAINTS

A. Problem Definition

Odometry estimation aims to calculate pose transformation $T = \{R, t\}$ between consecutive timesteps using sensor data, where R and t mean rotation and translation components. The source and target points $\mathcal{P} \in \{\mathcal{P}^s, \mathcal{P}^t\}$ are expressed as $\mathcal{P} = \{p_i = \{x_i, f_i\}\}_{i=1}^N$, where N is the number of points, $x \in \mathbb{R}^3$ means 3D coordinates, and $f \in \mathbb{R}^2$ denotes point feature with relative radial velocity (RRV) and radar cross section (RCS). For end-to-end odometry, a neural network Γ is used to encode inter-frame relationship and decode pose T . Unlike supervised learning using ground-truth pose (R^{gt}, t^{gt}) as a constraint to train model parameters θ , i.e., $\min_{\theta} \mathcal{L}(\Gamma_{\theta}(\mathcal{P}^s, \mathcal{P}^t), (R^{gt}, t^{gt}))$, we propose a hierarchical self-supervised loss with geometric ($\mathcal{L}_{cd}, \mathcal{L}_{co}$), temporal \mathcal{L}_{cm} and feature-level \mathcal{L}_{fc} terms, along with teacher guidance \mathcal{L}_{tg} and \mathcal{L}_{ga} , to generate comprehensive supervision signals. Our optimization objective is as follows:

$$\min_{\theta} (\mathcal{L}_{cd}(\hat{\mathcal{P}}^s, \mathcal{P}^t) + \mathcal{L}_{co}(\hat{\mathcal{P}}^s, \mathcal{P}^t) + \mathcal{L}_{tg}(T, T_{tg}) + \mathcal{L}_{ga}(\hat{\mathcal{P}}^s, \mathcal{P}^t) + \mathcal{L}_{fc}(\mathcal{F}^s, \mathcal{F}^t) + \mathcal{L}_{cm}(T_{k-2:k})), \quad (1)$$

where $\hat{\mathcal{P}}^s = \mathcal{T}(\mathcal{P}^s, T)$, and \mathcal{T} is the transformation operation. T_{tg} and $T_{k-2:k}$ are soft labels and sequential predicted poses.

B. Cluster-aware Network Architecture

Even though radar data is much sparser than LiDAR points, it possesses a block-like spatial distribution, making it easier to segment into distinct objects or regions based on geometric distances. These grouping labels then enable the integration of

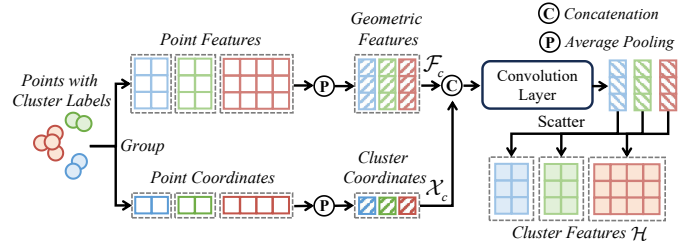


Fig. 4. Details of cluster feature generator. It takes point features with cluster labels as input to produce per-point cluster features.

instance features for matching, which reduces search space for potential matches and enhances outlier rejection by enforcing consistency within similar clusters. Motivated by this insight, we design a cluster-aware network structured as follows:

1) *Point-cluster Feature Encoder*: In Fig. 3, we first employ DBSCAN [41] to cluster raw points $\mathcal{P} \in \{\mathcal{P}^s, \mathcal{P}^t\}$ and assign cluster labels. Then, we utilize farthest point sampling (FPS) to unify two frames into the same number N of points and obtain the corresponding labels $\mathcal{C}^s, \mathcal{C}^t \in \mathbb{R}^N$. The set convolution layer [42] is further used to extract multi-scale features from downsampled points and combine them into $\mathcal{F}^s, \mathcal{F}^t \in \mathbb{R}^{N \times D}$ along channel dimension.

To acquire cluster information, we propose a cluster feature generator that exploits cluster labels to integrate point features and coordinates belonging to the same group to produce local geometric features \mathcal{F}_c and centroids \mathcal{X}_c of clusters. Both are concatenated and processed through two convolutional layers to obtain cluster features, which are then redistributed to their corresponding points, generating per-point cluster features \mathcal{H} . This process is illustrated in Fig. 4 and can be formulated as:

$$\mathcal{F}_c = \frac{1}{|\mathcal{C}_c|} \sum_{i \in \mathcal{C}_c} \mathcal{F}_i, \quad \mathcal{X}_c = \frac{1}{|\mathcal{C}_c|} \sum_{i \in \mathcal{C}_c} \mathcal{X}_i, \quad \forall c \in \{1, \dots, L\} \quad (2)$$

$$\mathcal{H}_i = \text{Conv}(\mathcal{F}_{c(i)} \oplus \mathcal{X}_{c(i)}), \quad \forall i \in \{1, \dots, N\} \quad (3)$$

where \mathcal{C}_c represents the set of points assigned to the cluster c , and L signifies the total number of clusters, while \mathcal{F}_i and \mathcal{X}_i denote the feature and coordinate of the i -th point from \mathcal{P} . Next, we leverage cost volume layers [43] to conduct feature correlation, which compares point pairs and learns the nonlinear relationship by MLP. However, rather than relying solely on point features, we employ cluster features \mathcal{H} to implement cluster-aware matching as described in Eq. 4. Since cluster features of the same object are similar in adjacent frames, this cue strengthens recognition of specific-object relationships and suppresses mismatches with irrelevant objects. We further aggregate cost features in a patch-to-patch manner [43], getting an inter-frame motion feature \mathcal{M} .

$$\text{Cost}(p_i^s, p_j^t) = \text{MLP}(f_i^s \oplus f_j^t \oplus h_i^s \oplus h_j^t \oplus (x_i^s - x_j^t)) \quad (4)$$

2) *Ego-motion Decoder*: To ensure the continuity of motion prediction, we first employ max-pooling to motion feature \mathcal{M} , obtaining a global motion representation $\mathcal{M}_g \in \mathbb{R}^D$. It is then merged with historical global feature using GRU [44], thereby constraining the current prediction using temporal consistency from adjacent states implicitly. The updated global feature is further combined with \mathcal{M} to form $\hat{\mathcal{M}} \in \mathbb{R}^{N \times 2D}$.

Unlike previous methods [5], [7], [31] that directly average motion features for pose prediction, we argue that focusing on critical points rather than all is necessary, as noisy points and dynamic objects cause errors in results. Thus, we calculate the confidence score of each point based on its geometric feature \mathcal{F} and motion feature \mathcal{M} , which implies density condition and movement relative to neighbours. The score-weighted feature is then used to estimate rotation R and translation t as follows:

$$W = \text{SoftMax}(\text{Conv}(\mathcal{F} \oplus \mathcal{M})) \quad (5)$$

$$R = \text{Conv} \sum_{i=1}^N (W_i \cdot \hat{\mathcal{M}}_i), \quad t = \text{Conv} \sum_{i=1}^N (W_i \cdot \hat{\mathcal{M}}_i) \quad (6)$$

C. Multi-level Self-supervised Signals

1) *Cluster-weighted Distance Loss*: Since radar points lack distinct structures (e.g., lines and planes), employing point relationship constraints for network learning is a basic approach. Specifically, the source points \mathcal{P}^s are transformed by T to $\hat{\mathcal{P}}^s$, where each \hat{p}_i^s is paired with its nearest neighbor $\hat{p}_j^t \in \mathcal{P}^t$, and their distances serve as supervision. To mitigate the impact of incorrect pairs caused by isolated and noisy points, we discard outliers using local density and define inter-frame distance as:

$$d_i^{s \rightarrow t} = \mathbb{I}(\rho(\hat{p}_i^s) > \delta) \max(\min_{p_j^t \in \mathcal{P}^t} \|\hat{p}_i^s - p_j^t\|_2^2 - \epsilon, 0) \quad (7)$$

where $\rho(\cdot)$ is a density function, while δ and ϵ mean the density and distance thresholds. Although averaging all distances d_i is convenient, this overlooks the contribution of different regions. For example, larger point clusters typically exhibit more stable and complete geometries across frames, enabling more precise consistency assessment than the fragmented clusters. Thus, we enhance point distances in large clusters and suppress those in small clusters through cluster labels \mathcal{C}_c as weighting factors:

$$\mathcal{L}_{cd}^{s \rightarrow t} = \sum_{c=0}^{L-1} \left(\frac{n_c}{N} \cdot \frac{1}{n_c} \sum_{i \in \mathcal{C}_c} d_i^{s \rightarrow t} \right), \quad \mathcal{L}_{cd} = \mathcal{L}_{cd}^{s \rightarrow t} + \mathcal{L}_{cd}^{t \rightarrow s} \quad (8)$$

where n_c indicates the number of points in the cluster labeled c . The bidirectional matching strategy is also used to eliminate ambiguity in unidirectional matching, as displayed in Fig. 3(a).

2) *Column Occupancy Loss*: While the point-to-point constraint facilitates network convergence, it is inherently difficult for matched pairs to correspond to identical physical locations in 3D space, resulting in geometric inconsistency. Meanwhile, distance uncertainty of point pairs caused by inaccurate radar measurement amplifies this issue. Thus, we propose a column occupancy loss in Fig. 3(b), whose core idea is to transform point clouds into voxel occupancy representation with a fixed resolution that has tolerance for position noise and fuzzy space correspondences. Subsequently, column-wise comparison enables a more reliable consistency evaluation by operating over a larger range, which effectively reduces the influence of local noise that often plagues small-scale point-pair comparisons.

Specifically, given a point cloud $\mathcal{P} \in \{\hat{\mathcal{P}}^s, \mathcal{P}^t\}$, we first map each point $p_i = (x_i, y_i, z_i)$ into a 2D polar representation by computing its azimuth angle θ_i and radial distance r_i :

$$\theta_i = 90 + \text{atan2}(y_i, x_i) \cdot \frac{180}{\pi}, \quad r_i = \sqrt{x_i^2 + y_i^2} \quad (9)$$

The angle θ_i and distance r_i are discretized into sectors and rings with the resolutions controlled by $\Delta_\theta = \frac{360^\circ}{N_s}$ and $\Delta_r = \frac{r_{\max}}{N_r}$, where N_s and N_r mean the number of sectors and rings. We then generate binary occupancy matrices $\mathcal{S} \in \{0, 1\}^{N_r \times N_s}$ for $\hat{\mathcal{P}}^s$ and \mathcal{P}^t , respectively. The element $\mathcal{S}(k, l)$ indicates the presence of at least one point in the k -th ring and l -th sector:

$$\mathcal{S}(k, l) = \mathbb{I} \left(\exists p_i \text{ s.t. } \left\lfloor \frac{r_i}{\Delta_r} \right\rfloor = k \text{ and } \left\lfloor \frac{\theta_i}{\Delta_\theta} \right\rfloor = l \right) \quad (10)$$

For the occupancy matrices from two frames, we calculate the cosine similarity between corresponding columns $\mathcal{S}^s[:, l]$ and $\mathcal{S}^t[:, l]$ to signify structural differences within a large receptive field. Columns where all elements are equal to 0 due to point sparsity and limited FOV are removed. The column occupancy loss is expressed as the average dissimilarity across all valid columns in Eq. 11, where \mathbb{L} is the non-empty column indices.

$$\mathcal{L}_{co} = 1 - \frac{1}{|\mathbb{L}|} \sum_{l \in \mathbb{L}} \frac{\mathcal{S}^s[:, l] \cdot \mathcal{S}^t[:, l]}{\|\mathcal{S}^s[:, l]\|_2 \cdot \|\mathcal{S}^t[:, l]\|_2} \quad (11)$$

3) *Teacher Guidance Loss*: Beyond the above losses, which propel model learning by rigid geometric alignment, we think that creating pseudo labels as soft supervision for the network can transfer some meaningful knowledge based on distillation learning theory [45], [46]. Meanwhile, unlike common distillation methods (e.g., [47]) that use a large network to generate pseudo labels for training a lightweight model, we propose a teacher guidance loss (Fig. 3(c)) that regards a geometry-based method as the teacher. It uses the network's predicted pose as an initial guess for the pose refinement. A selective distillation is then adopted to identify and discard unreliable poses, while using trustworthy ones as soft labels to drive model learning towards better geometric solutions.

Concretely, based on the transformed point cloud $\hat{\mathcal{P}}^s$ by T , we apply the distance-weighted Kabsch algorithm to solve the

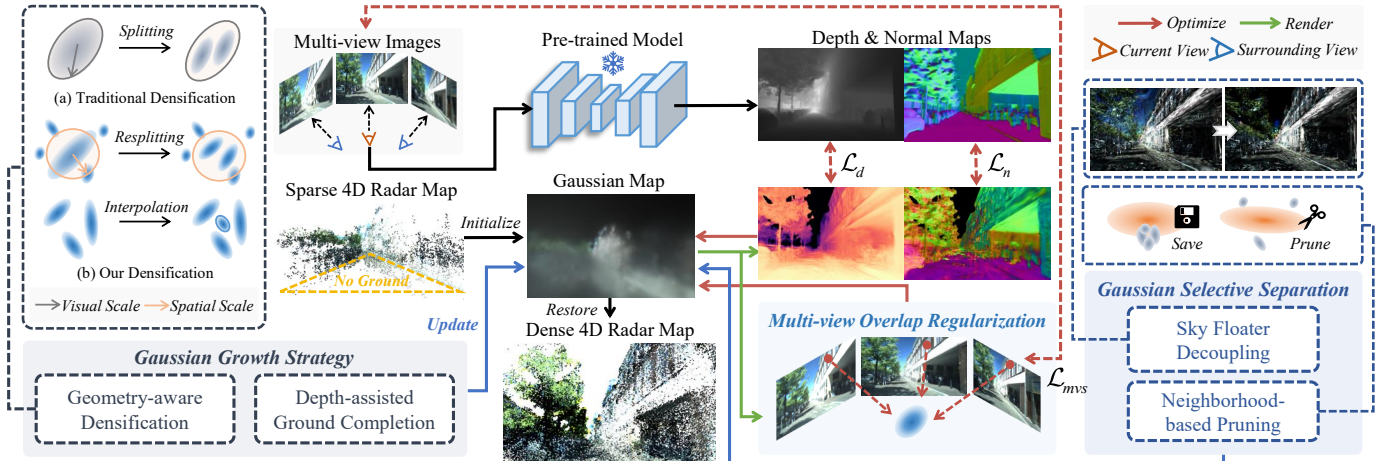


Fig. 5. Overview of gaussian-based map optimization. We first initialize a sparse 4D radar map as gaussians and perform attribute optimization by gradients derived from multi-view image rendering with the depth and normal maps. During optimization, we adopt ground completion and geometry-aware densification to grow the number of gaussians to reconstruct missing structure, while employing selective separation to decouple sky floaters and avoid excessive pruning. Finally, the optimized gaussians are restored into a dense radar map.

pose adjustment $\Delta T = \{\Delta R, \Delta t\}$ by minimizing the nearest neighbor distance between $\hat{\mathcal{P}}^s$ and \mathcal{P}^t , defined as:

$$d_{\max} = \max_i \left(\min_{p_j^t \in \mathcal{P}^t} \|\hat{p}_i^s - p_j^t\|_2 \right), w_i = \frac{d_{\max} - d_i}{d_{\max}} \quad (12)$$

$$\Delta T = \operatorname{argmin} \sum_{i=1}^N w_i \|\Delta R \hat{p}_i^s + \Delta t - \operatorname{NN}(\hat{p}_i^s, \mathcal{P}^t)\|_2^2 \quad (13)$$

where w_i and $\operatorname{NN}(\cdot)$ are the distance weight and nearest neighbor search, and the updated pose is $T_{tg} = \Delta T \cdot T = \{R_{tg}, t_{tg}\}$. Despite using T as an initial guess, the optimized pose T_{tg} may fail to improve on T because of the challenge posed by radar point sparsity to the Kabsch algorithm. Therefore, a selection mechanism is adopted to map \mathcal{P}^s to $\hat{\mathcal{P}}_{tg}^s$ by T_{tg} , and to convert $\{\hat{\mathcal{P}}^s, \hat{\mathcal{P}}_{tg}^s, \mathcal{P}^t\}$ into gaussian mixture models (GMMs) [48] and evaluate the alignment of GMMs through Cauchy-Schwarz (CS) divergence. When T_{tg} produces a lower CS divergence between the projected and target points \mathcal{P}^t compared to T , it can be regarded as a valid refined pose and applied to constrain the model training as follows:

$$M = \mathbb{I}(g(\mathcal{G}(\hat{\mathcal{P}}^s), \mathcal{G}(\mathcal{P}^t)) > g(\mathcal{G}(\hat{\mathcal{P}}_{tg}^s), \mathcal{G}(\mathcal{P}^t))) \quad (14)$$

$$\mathcal{L}_{tg} = M \cdot (\|R - R_{tg}\|_1 + \|t - t_{tg}\|_1) \quad (15)$$

where g and \mathcal{G} mean functions of CS divergence and gaussian mixture. As a result, selective guidance avoids forcing model to imitate erroneous poses. In addition, we use CS divergence of $\mathcal{G}(\hat{\mathcal{P}}^s)$ and $\mathcal{G}(\mathcal{P}^t)$ as a loss term \mathcal{L}_{ga} to drive model learning when there are no reliable soft labels available (i.e. $M = 0$).

4) *Feature Contrast Loss*: Apart from the result-level constraints, the feature-level regularization is also critical, as pose estimation relies on inter-frame feature correlation. Thus, we introduce a feature contrast loss in Fig. 3(d) to enhance feature discrimination among points and help perceive subtle motion between frames.

We initially consider the backbone's outputs \mathcal{F}^s and \mathcal{F}^t as feature sources. For each point $\hat{p}_i^s = (\hat{x}_i^s, f_i^s) \in \hat{\mathcal{P}}^s$, we define its nearest point $p_{j+}^t = (x_{j+}^t, f_{j+}^t) \in \mathcal{P}^t$ as a positive sample, whereas the farthest point $p_{j-}^t = (x_{j-}^t, f_{j-}^t)$ is selected as the

negative sample instead of neighboring points. This is because the neighbors' features are usually similar to \hat{p}_i^s , causing weak contrastive signals, which also may generate a false perception that neighbors exhibit larger discrepancies from \hat{p}_i^s than non-neighboring points. Thus, using the farthest point from a global perspective as a negative sample is more reasonable. Next, we use information noise contrastive estimation as a loss function:

$$j^+ = \operatorname{argmin}_{j \in [1, N]} \|\hat{x}_i^s - x_j^t\|_2, j^- = \operatorname{argmax}_{j \in [1, N]} \|\hat{x}_i^s - x_j^t\|_2 \quad (16)$$

$$\mathcal{L}_{fc} = -\frac{1}{N} \sum_{i=1}^N \log \frac{e^{s(f_i, f_{j+})/\tau}}{e^{s(f_i, f_{j+})/\tau} + e^{s(f_i, f_{j-})/\tau}} \quad (17)$$

where j^+ and j^- stand for the positive and negative sample indices. s represents the cosine similarity of features between point \hat{p}_i^s and its positive and negative samples. τ denotes the temperature coefficient.

5) *Continuous Motion Loss*: Supervised learning methods such as [31] implicitly model temporal motion by a network trained with continuous ground truth, which enforces predicted poses to conform to short-term motion patterns. However, for self-supervised learning, only relying on feature-level temporal fusion is still insufficient owing to missing explicit consecutive constraints. To address this issue, we apply the assumption of constant acceleration to ensure that the pose predictions maintain physical rationality. To be specific, we divide the training sequence into L -length frame segments and store the historical results in a buffer. For each predicted pose $T_k (2 \leq k < L)$ in the segment, we retrieve poses $\{T_{k-2}, T_{k-1}\}$ from the buffer and optimize the acceleration consistency for prediction stability utilizing \mathcal{L}_{cm} :

$$\alpha_k^R = (R_k - R_{k-1}), \alpha_k^t = (t_k - t_{k-1}), T_k = [R_k | t_k] \quad (18)$$

$$\mathcal{L}_{cm} = \lambda_{cm} (\max(\|\alpha_k^R - \alpha_{k-1}^R\|_1 - \epsilon^R, 0) + \max(\|\alpha_k^t - \alpha_{k-1}^t\|_1 - \epsilon^t, 0)) \quad (19)$$

where the relative rotation R_k is parameterized in Euler angles. To account for accelerated motion in real-world driving, we apply thresholds ϵ^R and ϵ^t to avoid too tight constraints, while enabling a gradual decay of the loss weight λ_{cm} for \mathcal{L}_{cm} .

IV. GAUSSIAN-BASED MAP OPTIMIZATION

A. Preliminary

The radar map is transformed into a representation signified by anisotropic gaussian ellipsoids G . Each gaussian contains its center $\mu \in \mathbb{R}^3$ in the world coordinate, opacity $o \in \mathbb{R}$, scale $S \in \mathbb{R}^3$, rotation $R \in \mathbb{R}^3$, and spherical harmonics $SH \in \mathbb{R}^3$. Here, μ corresponds to radar point coordinates. SH is obtained by mapping the RGB pixel values. S is initialized by distances to neighbors. The covariance matrix Σ is calculated to define the gaussian shape. Thus, the gaussian distribution is given by:

$$\Sigma = RSS^T R^T, \quad G(x) = e^{(-\frac{1}{2}(x-\mu)^T \Sigma^{-1}(x-\mu))} \quad (20)$$

Afterwards, given the transformation matrix $T_W^C = \{R_W^C, t_W^C\}$ between the camera and world coordinate systems, 3D gaussian ellipsoids (μ, Σ) in the world frame are projected onto the image plane as 2D gaussian (μ', Σ') by the following equation:

$$\mu' = \pi(T_W^C \cdot \mu), \quad \Sigma' = JR_W^C \Sigma (R_W^C)^T (J)^T \quad (21)$$

where R_W^C and t_W^C are the rotation and translation components. $J \in \mathbb{R}^{2 \times 3}$ is the Jacobian of the affine approximation of T_W^C . π means the 3D-to-2D projection operation. The influence of 2D gaussian on pixel $\rho = [u, v]^T$ is determined by weight α :

$$\alpha = o \cdot e^{(-\frac{1}{2}(\mu' - \rho)^T \Sigma'^{-1}(\mu' - \rho))} \quad (22)$$

Gaussians are then sorted by depth and rendered by volumetric α -blending to calculate the color of pixel ρ , as expressed by:

$$C(\rho) = \sum_{i=1}^n c_i \alpha_i \prod_{j=1}^{i-1} (1 - \alpha_j) \quad (23)$$

where c denotes the RGB color from spherical harmonics SH .

B. Gaussian Growth Strategy

1) *Depth-assisted Ground Completion*: Caused by specular reflection, the original radar map typically has fewer points on the ground compared to other areas (Fig. 5), posing a challenge for ground reconstruction with poor gaussian initialization. At the same time, standard gaussian densification in 3DGS [12] only generates a few ground gaussians for low-texture ground rendering in the image, leading to discontinuous ground in the optimized map (Fig. 6(a)). Thus, we propose a depth-assisted ground completion mechanism as described in Fig. 6(b), which integrates synthetic ground gaussians into optimization process through the depth estimation of the visual foundation model. The positions of these gaussians are adjusted through gradients from the differentiable rasterization to form a realistic ground in the final radar map. For optimization within a specific view, the ground completion consists of three steps:

a) *Virtual Points Generation*: DepthAnythingV2 [49] is first utilized to estimate a metric depth map \mathcal{D} of image \mathcal{I} from the current view, which is further mapped to the world coordinate by a transformation matrix T_W^C , generating virtual points \mathcal{P}_a .

b) *Ground Fitting*: We transform gaussians $G_b \subset G$ within the current view into points \mathcal{P}_b according to their center μ_b . Owing to the sparsity of ground points, we design an iterative RANSAC with normal-based filtering to fit an initial ground plane to \mathcal{P}_b . If the plane's normal departs from vertical, nearby

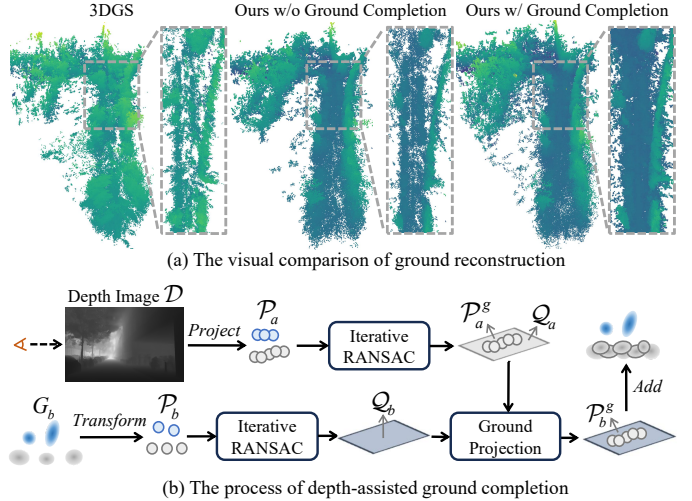


Fig. 6. The detail of depth-assisted ground completion and visual comparison.

outlier points are removed, and the plane is refitted until the normal approaches vertical direction. Afterwards, the resulting ground plane $Q_b = [n_b, d_b]$ is determined, where n_b and d_b are the normal vector and distance from the plane to the origin. For the virtual points \mathcal{P}_a , we apply the same approach to calculate $Q_a = [n_a, d_a]$ and nearby ground points \mathcal{P}_a^g .

c) *Ground Projection*: We obtain the rotation matrix R and translation t between planes via Rodrigues' rotation formula:

$$v = \hat{n}_a \times \hat{n}_b, \quad \hat{n}_a = \frac{n_a}{\|n_a\|_2}, \quad \hat{n}_b = \frac{n_b}{\|n_b\|_2} \quad (24)$$

$$R = I + [v]_{\times} + [v]_{\times}^2 \frac{1 - \hat{n}_a \cdot \hat{n}_b}{\|v\|_2^2}, \quad t = (d_a - d_b) \cdot \hat{n}_b \quad (25)$$

where $[v]_{\times}$ means the skew-symmetric matrix of v . Then, we incorporate new ground gaussians that are initialized from the projected points $\mathcal{P}_b^g = R \cdot \mathcal{P}_a^g + t$ into the original gaussian set G . Finally, by iteratively applying this process across multiple views, we achieve a dense reconstruction of ground structure.

2) *Geometry-aware Densification*: Due to the limited FOV and uneven distribution of radar points, initial gaussians only cover partial image regions, which forces them to be enlarged before being split into tile vacant regions. However, the common binary splitting (in Fig. 5(a)) struggles to efficiently deal with large-scale gaussians for rapid densification. Meanwhile, post-split positions are sampled from the rendering-optimized visual scales rather than physical spatial scales. This means the splitting results are tailored for image rendering but may fail to accurately restore the fine 3D structure. Thus, we present a geometry-aware splitting and interpolation scheme that yields gaussians adhering to local distributions and improves structural integrity.

For efficiency and a trade-off between image rendering and map quality, we extend initial splitting in [12] with a geometry-aware resplitting stage as illustrated in Fig. 5(b). This process operates on a subset G_s of G , which comprises I gaussians that still retain large scales S after the first splitting. For each G_s^i , we find its nearest gaussian G_s^j and use their distance as a spatial scale \hat{S}_i . Then, we sample the M offsets σ_i^m from a normal distribution with a mean of zero and variance of \hat{S}_i :

$$\hat{S}_i = \|\mu_i - \mu_j\|_2, \quad \{\sigma_i^m\}_{m=1}^M \sim \mathcal{N}(0, \hat{S}_i) \quad (26)$$

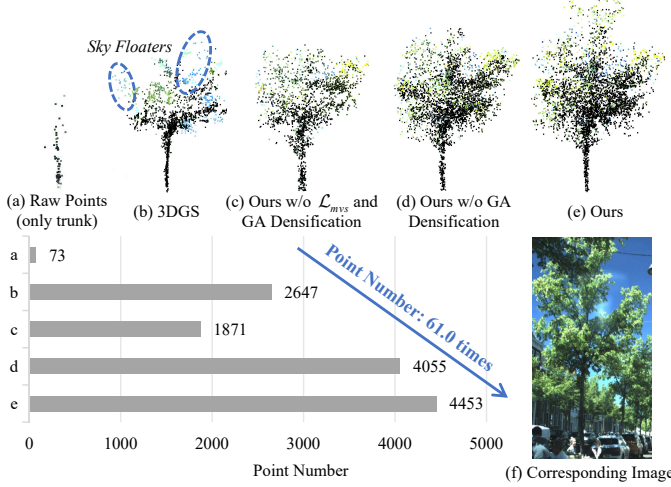


Fig. 7. Comparison of a tree reconstruction result by 3DGS and our method. We also display the total number of points to reveal the impact of our modules on structural integrity and density. GA is the abbreviation for geometry-aware.

Afterwards, the center μ_i of gaussian G_s^i is transformed using offset σ_i^m , and its scale S_i is decayed by ratio α . This parallel process generates $M \times I$ new gaussians from G_s , collectively denoted as $\hat{G}_s = \{\hat{G}_s^k\}_{k=1}^{M \times I}$. Upon creation of \hat{G}_s , the original set G_s is removed from G to eliminate redundancy, getting an updated gaussian set G' . This procedure is denoted as follows:

$$\hat{\mu}_k = \mu_i + R_i \sigma_i^m, \hat{S}_k = \alpha \cdot S_i, G' = (G \setminus G_s) \cup \hat{G}_s \quad (27)$$

Next, we adopt an interpolation strategy to improve the local density of gaussians. The gaussians $G_v \subset G$ with high opacity are first selected. For each G_v^i , a k -nearest neighbor set \mathcal{N}_i is constructed, and distant gaussians are discarded to produce $\hat{\mathcal{N}}_i$. Within the neighborhood, new ellipsoid centers $\hat{\mu}_i$ and colors \hat{c}_i are obtained through the following interpolation operation:

$$\hat{\mathcal{N}}_i = \{G_v^k \in \mathcal{N}_i \mid \|\mu_i - \mu_k\|_2 \leq d_{\max}\} \quad (28)$$

$$\hat{\mu}_i = \frac{1}{|\hat{\mathcal{N}}_i|} \sum_{G_v^j \in \hat{\mathcal{N}}_i} \mu_j, \hat{c}_i = \sum_{G_v^j \in \hat{\mathcal{N}}_i} \frac{\sum \|\mu_i - \mu_j\|_2}{\|\mu_i - \mu_j\|_2} \cdot c_j \quad (29)$$

In the end, we incorporate new gaussians \hat{G}_v into the original gaussians G to fill the void of local structures.

C. Gaussian Selective Separation

1) *Sky Floater Decoupling*: Radar map inherently contains virtual structures formed by noise, where the gaussians initialized from these artifacts are usually projected into sky regions and undergo splitting, resulting in numerous floaters near the actual structures. In addition, as shown in Fig. 7(b, f), the area that intersects with the sky in the image also tends to produce sky floaters. To solve these problems, we maintain a sky mask $\mathcal{M}_{\text{sky}}^{3D} \in \{0, 1\}^N$ (in Fig. 8), which is updated gradually as new sky gaussians appear by splitting or existing ones are pruned during the optimization process. To determine which gaussian ellipsoids belong to the sky, we feed the current image \mathcal{I} into MaskFormerv2 [50] to yield a 2D mask $\mathcal{M}_{\text{sky}}^{2D} \in \{0, 1\}^{H \times W}$, where H and W are the image height and width. We then

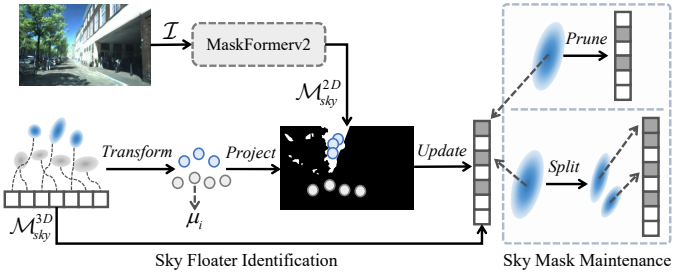


Fig. 8. The procedures of sky floater identification and sky mask maintenance.

project the center μ_i of each gaussian to the image plane, and update the mask $\mathcal{M}_{\text{sky}}^{3D}$ by the corresponding values in $\mathcal{M}_{\text{sky}}^{2D}$:

$$(u_i, v_i) = \Pi(\mu_i), \mathcal{M}_{\text{sky}}^{3D}(i) = \mathcal{M}_{\text{sky}}^{2D}(\lfloor u_i \rfloor, \lfloor v_i \rfloor) \quad (30)$$

where $\Pi(\cdot)$ and (u_i, v_i) mean the projection operator and pixel coordinates. As a result, unlike directly deleting sky gaussians, our decoupling strategy using a mask not only reduces floaters in the final radar map but also ensures that sky information is not lost during image rendering.

2) *Neighborhood-based Pruning*: As noted in Sec. IV-B2, uneven distribution of radar points causes oversized gaussians during the initial phase, later shrunk through splitting. However, most approaches directly remove all large gaussians at a fixed interval, which will mistakenly prune gaussians that are waiting to be split to recover the missing structure beyond the radar FOV. Fortunately, we notice that valuable large gaussians usually extend from existing structures with denser neighbors. Building upon this, we present a neighborhood-based pruning criterion \mathcal{M}_p that determines whether the gaussians should be removed by incorporating spatial relationships. Specifically, a gaussian is discarded when its average center distance relative to neighbors exceeds a threshold τ_d , and either its scale S_i or projected 2D radius r_i^{2D} surpasses thresholds τ_s or τ_r :

$$\mathcal{M}_p = \mathbb{I}(d(\mu_i) > \tau_d) \wedge (\mathbb{I}(S_i > \tau_s) \vee \mathbb{I}(r_i^{2D} > \tau_r)) \quad (31)$$

where $d(\cdot)$ denotes the KNN-distance function. In this way, the large gaussians utilized for subsequent completion are avoided from being deleted incorrectly.

D. Multi-view Overlap Regularization

Existing methods [12], [33], [35] usually optimize gaussians by minimizing the photometric loss between the single-view rendered image $\hat{\mathcal{I}}_t$ and the ground truth \mathcal{I}_t . However, geometric ambiguity in single-view observations makes it challenging for both the initial gaussians (with radar noise) and the post-split ones to shift quickly to accurate spatial locations, while risking overfitting in their distribution. We thus present a multi-view overlap regularization that renders images $\hat{\mathcal{I}}_{t+w}$ ($w \in \{-2L, -L, L, 2L\}$) from nearby timesteps and compares them with \mathcal{I}_{t+w} as additional supervision signals for gaussians in the current view. Since co-visible regions \mathcal{A}_{t+w} typically exist between $\hat{\mathcal{I}}_{t+w}$ and $\hat{\mathcal{I}}_t$, and satisfy an overlap relationship $\bigcup \mathcal{A}_{t+w} = \hat{\mathcal{I}}_t$ in most cases, this means that the corresponding gaussians for $\hat{\mathcal{I}}_t$ are constrained by at least two perspectives, as shown in Fig. 5. Thus, gaussian positions and other attributes can be optimized toward unambiguous states more easily. The

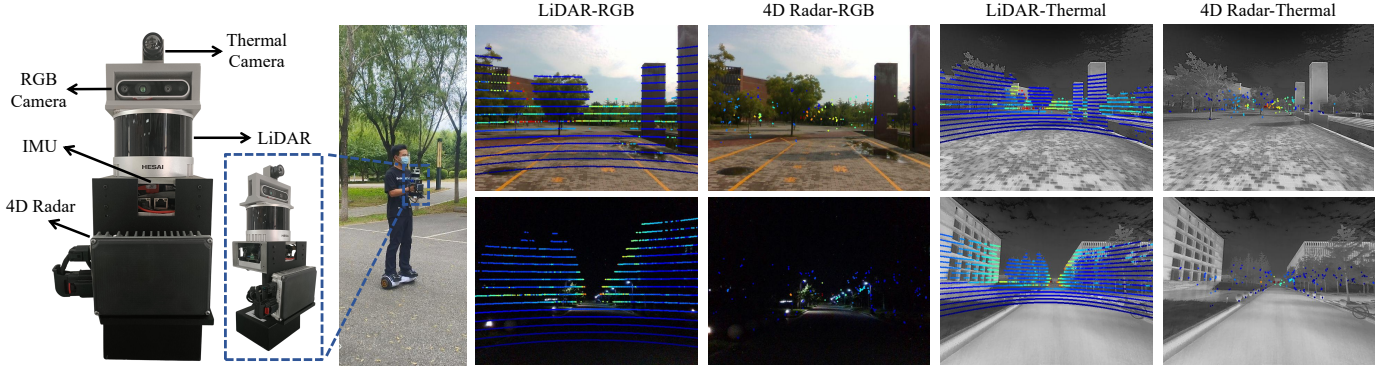


Fig. 9. The visualization of our handheld equipment and the projection results among different sensors. Multi-sensor data are collected across various campus scenes under both daytime and nighttime conditions.

multi-view overlap regularization is defined by the following functions:

$$\mathcal{L}_c = \frac{1-\lambda}{N} \sum_{i=1}^N |\hat{\mathcal{I}}_t^i - \mathcal{I}_t^i|^\gamma + \lambda \mathcal{L}_{\text{SSIM}}(\hat{\mathcal{I}}_t, \mathcal{I}_t) \quad (32)$$

$$\mathcal{L}_{mvc} = \frac{\lambda_{mvc}}{4} \sum_{i=1}^4 \mathcal{L}_c(\hat{\mathcal{I}}_{t+wi}, \mathcal{I}_{t+wi}) + \mathcal{L}_c(\hat{\mathcal{I}}_t, \mathcal{I}_t) \quad (33)$$

where $\lambda = 0.1$, $\lambda_{mvc} = 3.0$ indicate the loss weights, and we adopt L1 loss with exponential weight to strengthen the fitting on difficult samples. We also intuitively exhibit the influence of multi-view overlap regularization in Fig. 7(c, d).

E. Loss Functions

Except for multi-view regularization, we apply prior knowledge derived from visual fundamental models [49], [51] to optimize the geometric distribution of gaussians. We first render depths $\hat{\mathcal{D}}$ and normals $\hat{\mathcal{N}}$ through Eq. 34. We then supervise depths $\hat{\mathcal{D}}$ with L1 loss against the predicted depths \mathcal{D} obtained from DepthAnythingv2 [49], while adopting Metric3D [51] to get normals \mathcal{N} for regularizing $\hat{\mathcal{N}}$ by normal similarity loss. Both losses are defined in Eq. 35.

$$\hat{\mathcal{D}} = \sum_{i=1}^n d_i \alpha_i \prod_{j=1}^{i-1} (1 - \alpha_j), \quad \hat{\mathcal{N}} = \sum_{i=1}^n n_i \alpha_i \prod_{j=1}^{i-1} (1 - \alpha_j) \quad (34)$$

$$\mathcal{L}_d = \|(\mathcal{D} - \hat{\mathcal{D}})\|_1, \quad \mathcal{L}_n = 1 - \mathcal{N} \cdot \hat{\mathcal{N}} \quad (35)$$

To sum up, the overall loss function is formulated as follows:

$$\mathcal{L} = \mathcal{L}_{mvc} + \mathcal{L}_n + \mathcal{L}_d \quad (36)$$

where \mathcal{L}_{mvc} means the multi-view overlap regularization loss (Eq. 33), enforcing consistency of gaussian attributes across multiple views to resolve spatial ambiguity. Then, \mathcal{L}_n and \mathcal{L}_d incorporate monocular geometric priors to guide the gaussians towards forming accurate local structures and smooth surfaces.

V. EXPERIMENT

A. Datasets

To thoroughly evaluate our method, we conduct comprehensive experiments not only on public datasets, including View-of-Delft [52] and NTU4DRadLM [9], but also on our self-collected campus dataset to assess both odometry estimation accuracy and map optimization performance in various scenes. The details of the used datasets are shown in Tab. I.

TABLE I
THE DETAILS OF THE USED DATASETS. 3DL: 3D LiDAR, 4DR: 4D RADAR, VC: VISUAL CAMERA, TC: THERMAL CAMERA. DENSITY DENOTES THE DENSITY OF RADAR POINTS IN EACH FRAME.

Dataset	Sensors		Scenes		Density	Radar Frame#	Sequence#	
	3DL	4DR	VC	TC				
VoD [52]	✓	✓	✓		✓	Low	8,693	24
NTU [9]	✓	✓	✓	✓	✓	High	61,233	6
Ours	✓	✓	✓	✓	✓	Low	38,892	10

1) *View-of-Delft*: The VoD dataset [52] provides synchronized multi-sensor data, consisting of 64-beam LiDAR, RGB camera and 4D radar measurements captured in complex urban traffic environments. With a total of 8,693 frames, the dataset is structured into 24 continuous sequences. Consistent with the data partitioning scheme of [6], we divide these sequences into 13 for training, 4 for validation, and 7 for testing. Since each radar frame contains only 300-500 points, VoD presents severe challenges for odometry estimation and map optimization.

2) *NTU4DRadLM*: The NTU4DRadLM dataset [9] is collected using an Oculii Eagle 4D radar, Livox Horizon LiDAR, an RGB camera, and a thermal camera, which are not time-synchronized. It captures six trajectories across NTU campus, including structured, semi-structured, and unstructured scenarios. Data are collected from both a handcart platform moving at around 1m/s and vehicle-mounted systems traveling at 25-30km/h. For odometry estimation, we partition the sequences into training (*Garden*, *Nyl*, *Loop1*), validation (*Loop2*), and testing (*Loop3*, *Cp*) sets. In particular, the radar point clouds in NTU4DRadLM exhibit a higher density relative to the VoD dataset, typically comprising thousands of points per frame.

3) *Self-Collected Campus Dataset*: To conduct more extensive experiments, we build a handheld data collection system that is more compact and portable compared to the handcart platform in NTU4DRadLM. Our system integrates a 16-beam LiDAR, GPAL 4D radar, RGB camera, thermal camera, and IMU. Here, the 4D radar operates at around 15 Hz and collects around 500 points per frame. The setup of our multi-sensor equipment and the projection of the point cloud onto the image are shown in Fig. 9. Using this platform, we build a campus dataset with 8 daytime sequences and 2 nighttime sequences under various scenes. For daytime sequences (34,241 frames total), we divide them into training, validation, and testing sets based on a 6:1:3 ratio. The validation set (*Gym*) includes 3,124 frames, while the testing set (*Building2*, *Parking2*, *Straight*)

TABLE II
4D RADAR ODOMETRY EXPERIMENT RESULTS ON VIEW-OF-DELFIT (VOD) DATASET.

Method	03		04		09		17		19		22		24		Mean		
	t_{rel}	r_{rel}	t_{rel}	r_{rel}	t_{rel}	r_{rel}	t_{rel}	r_{rel}	t_{rel}	r_{rel}	t_{rel}	r_{rel}	t_{rel}	r_{rel}	t_{rel}	r_{rel}	
Classical-based	ICP-po2po	0.39	1.00	0.21	1.14	0.15	0.72	0.16	0.53	1.40	4.70	0.44	0.76	0.24	0.77	0.43	1.37
	ICP-po2pl	0.42	2.19	0.37	1.83	0.50	1.32	0.23	0.68	3.04	5.62	0.42	1.20	0.35	0.67	0.76	1.93
	GICP	0.46	0.68	0.30	0.39	0.51	0.32	0.40	0.10	0.51	1.23	0.34	0.57	0.15	0.30	0.38	0.51
	NDT	0.55	1.60	0.47	0.91	0.46	0.56	0.44	0.40	1.33	2.58	0.47	1.10	0.36	1.84	0.58	1.28
LiDAR-based	Full A-LOAM	NA	NA	0.03	0.09	0.04	0.19	0.02	0.04	0.38	1.35	0.06	0.18	0.06	0.20	0.10	0.34
	A-LOAM w/o mapping	NA	NA	0.14	0.35	0.16	1.23	0.09	0.26	1.17	4.63	0.27	0.92	0.16	0.81	0.33	1.37
	LO-Net	1.05	1.78	0.26	0.49	0.30	0.36	0.57	0.14	3.29	3.07	1.00	1.12	0.77	1.45	1.03	1.20
	PWCLO-Net	0.26	0.37	0.31	0.40	0.38	0.55	0.27	0.39	1.23	0.91	0.23	0.35	0.46	0.82	0.45	0.54
4D Radar-based Supervised	CMFlow	0.06	0.10	0.05	0.09	0.09	0.14	0.06	0.03	0.28	0.94	0.14	0.29	0.12	0.58	0.11	0.31
	4DRO-Net	0.08	0.10	0.04	0.07	0.13	0.38	0.09	0.10	0.91	0.62	0.23	0.32	0.28	1.20	0.25	0.40
	CAO-RONet	0.05	0.03	0.04	0.04	0.06	0.09	0.10	0.01	0.02	0.05	0.08	0.06	0.14	0.08	0.07	0.05
	DNOI-4DRO	0.02	0.02	0.02	0.03	0.02	0.02	0.02	0.02	0.02	0.04	0.03	0.02	0.03	0.05	0.02	0.03
4D Radar-based Self-supervised	RaFlow	0.87	2.09	0.07	0.44	0.11	0.09	0.13	0.03	1.22	4.09	0.72	1.34	0.25	1.14	0.48	1.32
	Ours	0.04	0.07	0.04	0.03	0.04	0.05	0.03	0.02	0.04	0.04	0.06	0.10	0.12	0.05	0.05	0.05

TABLE III

4D RADAR ODOMETRY EXPERIMENT RESULTS ON VOD DATASET USING THE SAME CONFIGURATION AS SELFRO. BLUE AND RED ARE USED TO DISTINGUISH **SUPERVISED** AND **SELF-SUPERVISED** METHODS.

Method	00		03		04		07		23		Mean	
	t_{rel}	r_{rel}										
CMFlow	0.04	0.05	0.07	0.09	0.06	0.09	0.03	0.04	0.09	0.14	0.06	0.08
4DRO-Net	0.08	0.03	0.06	0.05	0.08	0.07	0.05	0.03	0.10	0.15	0.07	0.07
CAO-RONet	0.05	0.03	0.02	0.03	0.03	0.05	0.02	0.02	0.04	0.06	0.03	0.04
RaFlow	0.61	0.84	0.87	1.98	0.07	0.45	0.07	0.04	0.42	1.16	0.41	0.90
SelfRO	0.07	0.11	0.10	0.16	0.05	0.13	0.07	0.14	0.13	0.14	0.08	0.14
Ours	0.03	0.04	0.04	0.07	0.03	0.03	0.01	0.02	0.05	0.04	0.03	0.04
Impr. (%)	57.1	63.6	60.0	56.3	40.0	76.9	85.7	50.0	61.5	71.4	62.5	71.4

TABLE IV

4D RADAR ODOMETRY EXPERIMENT RESULTS ON NTU4DRADLM. “R” AND “A” MEAN THE RELATIVE POSE ERROR (RPE) AND ABSOLUTE TRAJECTORY ERROR (ATE), RESPECTIVELY.

Method	Loop2 (4.79km)			Loop3 (4.23km)			Cp (0.25km)		
	R (m)	R (°)	A (m)	R (m)	R (°)	A (m)	R (m)	R (°)	A (m)
ICP	12.357	8.003	613.073	13.772	3.818	304.793	0.543	1.274	3.639
NDT	3.406	5.775	652.073	2.798	3.579	169.034	0.223	1.368	3.294
GICP	2.448	2.517	58.155	3.161	2.052	29.224	0.192	1.184	2.256
APDGICP	2.459	2.616	145.674	3.072	2.209	27.871	0.216	1.241	2.408
CAO-RONet	1.504	4.215	265.864	4.228	2.604	481.916	0.342	2.471	15.557
RaFlow	NA	NA	NA	NA	NA	NA	1.310	9.367	44.228
Ours	1.521	2.448	38.876	2.104	1.769	22.077	0.248	1.121	1.749

contains 9,701 frames. Moreover, nighttime sequences are utilized to evaluate the performance of thermal image rendering and map optimization in low-light conditions.

B. Implementation Details

1) *Data Processing*: For odometry data preprocessing, we first apply a height-based filtering to the point clouds, retaining only those points within the vertical range of [-3m, 3m]. To augment the training data diversity in the VoD dataset, we flip training sequences to generate reversed-motion data. Random translations within ± 1 m along each axis are also employed to point clouds during training. For DBSCAN-based clustering, we use a 3-meter search radius and a minimum cluster size of 3 points for VoD and self-collected datasets, while configuring a 1.5-meter radius and a 5-point minimum for NTU4DRadLM. In the map optimization pipeline, we downsample the points of radar maps in the NTU4DRadLM to 25% of their original

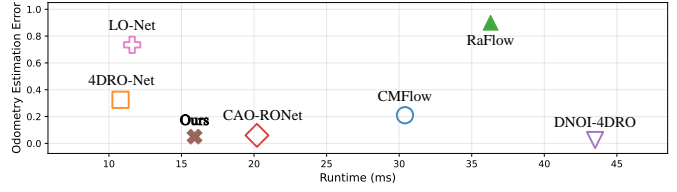


Fig. 10. Comparison of runtime and odometry estimation error across several methods on Delft dataset. The error is computed as the mean of r_{rel} and t_{rel} . Our method achieves an optimal balance between performance and efficiency.

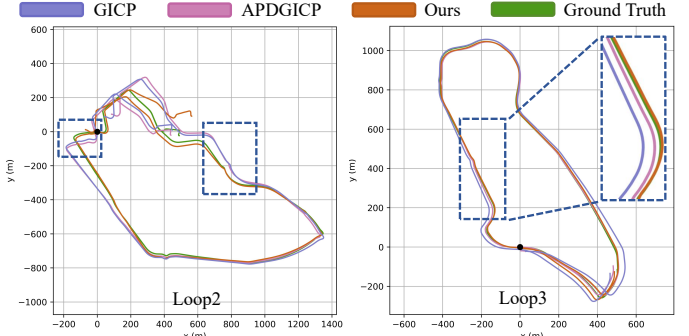


Fig. 11. The trajectory visualization on the long sequences of NTU4DRadLM. density for gaussian initialization and select image keyframes at a 5-frame interval to optimize maps. For the VoD dataset, no sampling is applied to either images or point clouds.

2) *Network Training & Gaussian Optimization*: For odometry, our model is trained for 60 epochs on a single NVIDIA RTX 4090 GPU through the Adam optimizer with a batch size of 24. Meanwhile, we assign an initial learning rate of 1×10^{-3} with a per-epoch decay rate of 0.9 and employ equal weights for all self-supervised loss terms. For map optimization, the gaussian parameters are updated utilizing Adam optimizer for 15,000 iterations, with gaussian densification every 100 steps starting at iteration 500 with 5×10^{-4} gradient threshold.

3) *Evaluation Metrics*: For odometry evaluation on the VoD, we adopt the relative pose error (RPE) metric, following previous methods [5], [6], [31]. With this metric, we calculate the root mean square error (RMSE) for rotation ($^{\circ}/m$) and translation (m/m), with 20m intervals ranging from 20m to 160m. For the NTU4DRadLM and self-collected datasets, we employ the same approach as 4DRadarSLAM [1] to evaluate absolute trajectory error (ATE) and RPE. In our self-collected

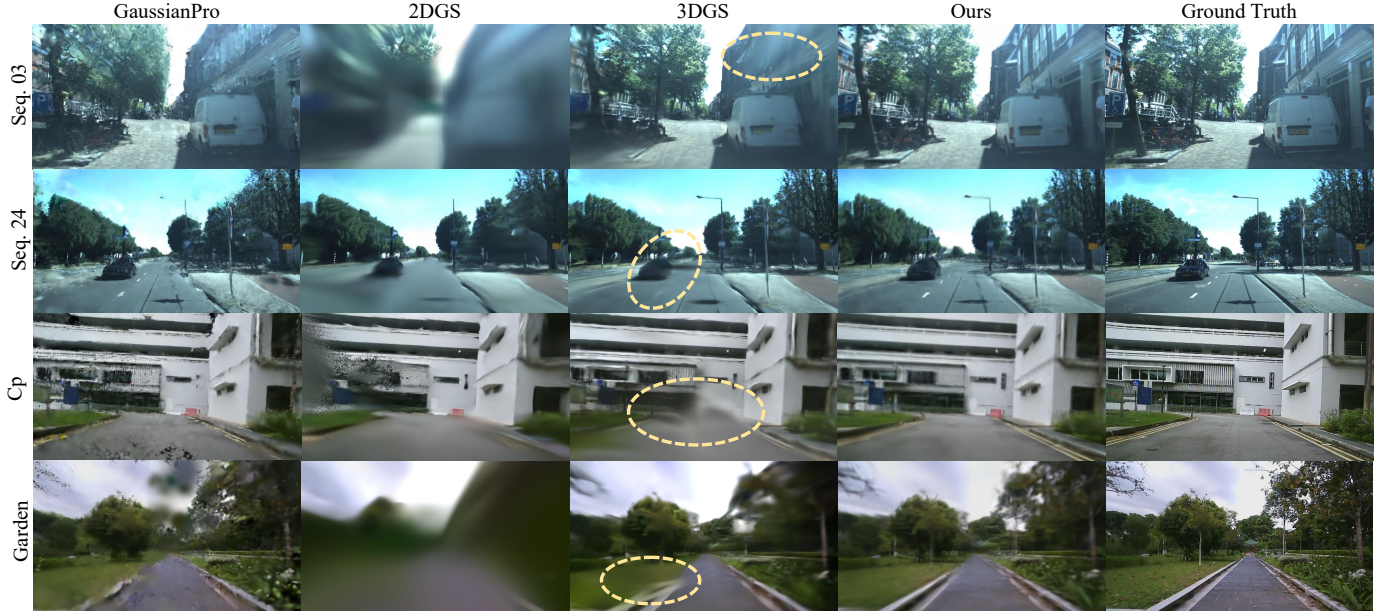


Fig. 12. Qualitative comparisons of rendering quality on the VoD and NTU4DRadLM datasets. We mark poor rendering regions of 3DGS with yellow circles.

TABLE V

THE PERFORMANCE OF MAP OPTIMIZATION AND IMAGE RENDERING ON VIEW-OF-DELFT (VOD) DATASET. “ODOM” IS DEFINED AS USING POSES ESTIMATED BY OUR SELF-SUPERVISED ODOMETRY TO CONSTRUCT INITIAL RADAR MAPS.

Method	03			04			09			22			24		
	F-Score↑	CD↓	MHD↓												
GaussianPro	0.378	1.482	1.148	0.297	1.881	1.486	0.253	2.514	1.801	0.357	1.481	0.975	0.241	3.085	6.817
2DGS	0.271	1.441	1.316	0.263	1.092	0.537	0.254	1.113	0.358	0.186	1.422	0.704	0.125	2.827	17.587
3DGS	0.339	1.171	1.642	0.351	0.951	0.721	0.364	0.987	0.589	0.349	1.171	0.831	0.318	1.728	1.485
Ours	0.509	0.955	0.271	0.501	0.733	0.164	0.556	0.624	0.105	0.571	0.664	0.099	0.428	1.128	0.304
3DGS (Odom)	0.208	1.507	3.983	0.285	1.229	0.977	0.311	1.049	0.918	0.241	1.548	1.923	0.254	1.809	3.017
Ours (Odom)	0.394	1.196	0.670	0.438	0.731	0.188	0.389	0.892	0.267	0.433	1.083	0.473	0.402	1.161	0.352
	PSNR↑	SSIM↑	LPIPS↓												
GaussianPro	15.783	0.494	0.488	18.721	0.647	0.391	16.805	0.664	0.434	17.171	0.615	0.466	20.551	0.733	0.339
2DGS	14.713	0.469	0.569	17.877	0.641	0.433	16.849	0.669	0.454	14.901	0.582	0.514	21.235	0.744	0.369
3DGS	15.965	0.505	0.511	19.184	0.666	0.389	18.271	0.696	0.408	16.727	0.609	0.476	21.858	0.762	0.321
Ours	19.473	0.571	0.453	21.366	0.683	0.371	20.862	0.725	0.387	20.938	0.659	0.432	24.208	0.787	0.316
3DGS (Odom)	15.702	0.504	0.516	19.002	0.661	0.397	17.956	0.693	0.413	16.631	0.605	0.488	21.845	0.760	0.323
Ours (Odom)	19.306	0.561	0.467	21.295	0.681	0.376	20.821	0.724	0.388	20.879	0.657	0.438	24.218	0.788	0.316

dataset, we use FAST-LIO [53] as the ground-truth trajectory because of the multipath errors caused by tree and building obstructions, which will degrade the accuracy of RTK GPS. For map quality assessment, we construct LiDAR maps as ground truth and follow previous point cloud completion approaches, such as [10], [11], to utilize the L1 Chamfer Distance (CD), Modified Hausdorff Distance (MHD), and F-Score (with a distance threshold of $0.3m$) as metrics for comprehensive evaluation. Furthermore, to evaluate image rendering quality, we adopt three metrics, namely the peak signal-to-noise ratio (PSNR), learned perceptual image patch similarity (LPIPS), and structural similarity index measure (SSIM), as utilized in 3DGS [12].

C. Performance Comparisons on Public Datasets

1) *4D Radar Odometry*: As displayed in Tab. II, since each radar frame of the VoD dataset only includes 300-500 points, classical approaches such as ICP-po2po, ICP-po2pl, GICP, and NDT are difficult to find sufficient geometric correspondences for pose estimation, resulting in unsatisfactory results. Besides,

the differences in sensor characteristics make it challenging for the geometric-based method (A-LOAM [17]) and learning-based algorithms (LO-Net [54] and PWCLO-Net [20]) designed for LiDAR to be applicable to 4D radar. Among radar-based learning works, our self-supervised framework surpasses RaFlow [8] notably based on constraints from various aspects and reduces the gap compared to supervised learning methods obviously in a label-free manner. Besides, as shown in Fig. 10, our self-supervised approach runs at $15.9ms$, outperforming supervised CAO-RONet [31] ($20.2ms$) and DNOI-4DRO [55] ($43.2ms$). In Tab. III, since SelfRO [7] is not open-sourced, we employ the same sequence division protocol as described in its paper to train our model for a fair comparison. The results validate the superiority of our method over SelfRO.

Due to lacking time synchronization in NTU4DRadLM, we first perform an interpolation operation to compute the ground-truth poses corresponding to the 4D radar timestamps and then train CAO-RONet [31]. However, the results in Tab. IV show that [31] suffers from poor performance, implying that supervised algorithms heavily rely on precise time synchronization

TABLE VI

THE EVALUATION OF MAP OPTIMIZATION AND IMAGE RENDERING ON NTU4DRADLM. GSPro IS THE ABBREVIATION FOR GAUSSIANPRO.

Method	Cp (Structured)			Garden (Unstructured)			Nyl (Semi-structured)		
	F-Score↑	CD↓	MHD↓	F-Score↑	CD↓	MHD↓	F-Score↑	CD↓	MHD↓
GSPro	0.297	3.512	3.212	0.501	0.877	0.221	0.198	2.087	1.384
2DGS	0.222	1.109	1.219	0.287	1.037	0.268	0.061	2.073	1.723
3DGS	0.382	1.104	0.521	0.545	0.749	0.132	0.228	2.592	2.039
Ours	0.615	0.692	0.091	0.688	0.467	0.041	0.372	1.016	0.345
	PSNR↑	SSIM↑	LPIPS↓	PSNR↑	SSIM↑	LPIPS↓	PSNR↑	SSIM↑	LPIPS↓
GSPro	17.411	0.546	0.506	15.908	0.473	0.547	14.793	0.466	0.604
2DGS	17.363	0.555	0.519	14.741	0.461	0.625	14.456	0.474	0.613
3DGS	18.385	0.578	0.466	17.635	0.521	0.544	15.319	0.488	0.591
Ours	19.821	0.601	0.445	19.608	0.549	0.502	18.788	0.536	0.529

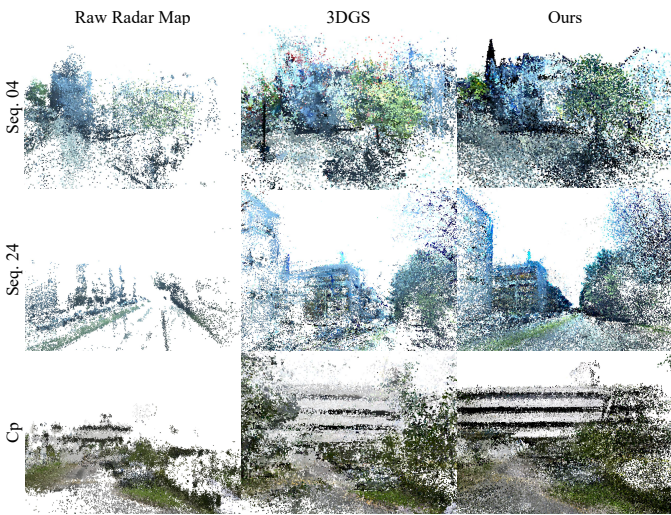


Fig. 13. Visualization of the optimized radar maps. Our algorithm generates denser and more complete scenes compared to 3DGS.

and accurate poses as supervision signals. In contrast, our self-supervised method breaks free from these limitations and still works well. Especially for long sequences (*Loop2* and *Loop3*) with 4.79 km and 4.23 km , we achieve ATE of 38.876m and 22.077m , representing a reduction of 73% and 21% compared to APDGICP [1] (145.674m and 27.871m), respectively.

In addition, Fig. 11 further demonstrates that our trajectories in kilometer-level sequences are closer to the ground truth than traditional GICP and APDGICP designed for 4D radar, especially in rotation. This improvement could be attributed to our method’s ability to learn effective inter-frame correspondence through multi-level constraints, including noise-tolerant geometric consistency, teacher guidance, feature contrast, and constant-acceleration motion modeling. And the effectiveness of these constraints is validated in ablation studies (Sec. V-D1). We also show more visualizations of trajectories based on our self-collected dataset in Fig. 18.

2) *Map Optimization*: In this part, we select five sequences from test sets of the VoD dataset, then use ground-truth poses and predicted odometry to build initial radar maps respectively. The former isolates map optimization from odometry errors, enabling a more focused and pure evaluation of our proposed method. The radar maps are further optimized by differentiable rasterization. The results in Tab. V indicate that our algorithm achieves better geometric accuracy in the reconstructed maps, with mean CD and MHD of 0.821 and 0.189, considerably

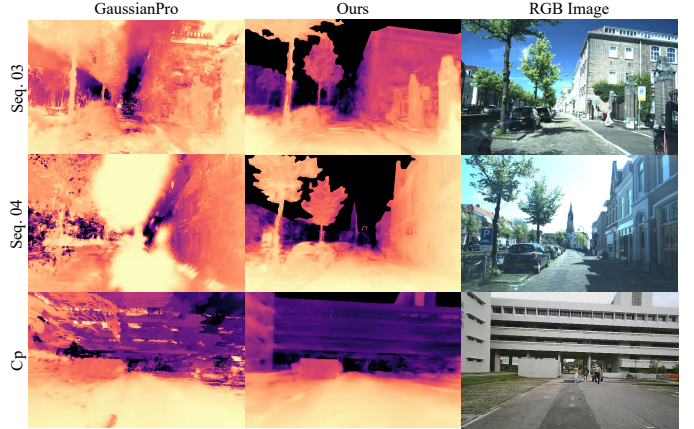


Fig. 14. The visualization of rendered depths. Our depth maps show smoother surfaces, proving the superior geometric quality of reconstructed maps.

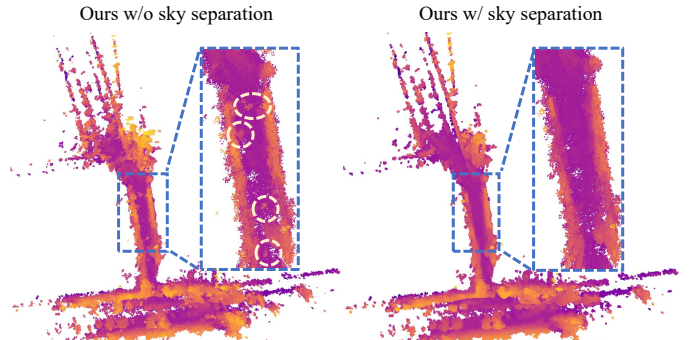


Fig. 15. The effect of sky separation. Floaters are marked using yellow circles.

lower than that of 3DGS [12] (1.202 CD and 1.054 MHD). We attribute these advantages to geometry-aware densification for dense structure generation, selective separation for precise gaussian pruning, and the multi-view regularization for optimization with reduced ambiguity. Then, these well-distributed gaussians enable accurate scene representation, consequently resulting in superior rendering quality compared with previous approaches [12], [33], [35]. Moreover, we conduct experiments on NTU4DRadLM across diverse scenes in Tab. VI, showing that our method maintains obvious advantages in map quality and rendering fidelity relative to other algorithms.

As shown in Fig. 12, our method achieves a higher-fidelity rendering of environmental details. Especially, it better reconstructs building extending beyond the radar’s FOV and ground with weak initialization, because of the proposed densification strategy. To intuitively demonstrate reconstruction results, we present the original input and optimized radar maps in Fig. 13. Although 3DGS recovers missing structures to some extent, the resulting geometry remains a sparse distribution with fuzzy artifacts. In comparison, our approach reconstructs maps with clearer structures and higher point density using radar-specific optimization, while ground surfaces are also restored by depth-assisted completion. Furthermore, we show the rendered depth maps in Fig. 14, which demonstrates that our method produces smoother surfaces and higher local consistency.

D. Ablation Studies

In this section, we conduct ablation studies through progressively adding modules and replacing core strategies to evaluate

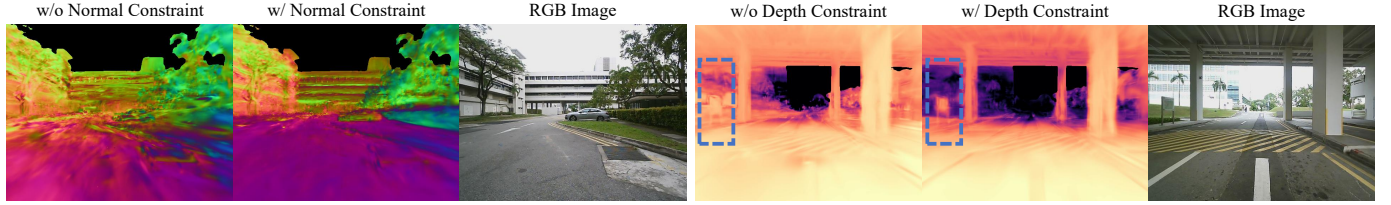


Fig. 16. Effects of normal and depth constraints. Results display that the former smooth surfaces, while the latter enhance the spatial accuracy of structures.

TABLE VII

THE EFFECTS OF DIFFERENT SELF-SUPERVISED LOSS TERMS.

\mathcal{L}_{cd}	\mathcal{L}_{co}	\mathcal{L}_{ga}	\mathcal{L}_{tg}	\mathcal{L}_{fc}	\mathcal{L}_{cm}	Cluster	Mean t_{rel}	Mean r_{rel}
✓						✓	0.219	0.332
✓	✓					✓	0.190	0.235
✓	✓	✓				✓	0.124	0.175
✓	✓	✓	✓			✓	0.078	0.091
✓	✓	✓	✓	✓		✓	0.056	0.068
✓	✓	✓	✓	✓	✓		0.068	0.108
✓	✓	✓	✓	✓	✓	✓	0.053	0.053

TABLE VIII

THE EFFECTS OF OUR SELF-SUPERVISED STRATEGY SELECTION.

Strategy	Mean t_{rel}	Mean r_{rel}
\mathcal{L}_{cd} : w/o Cluster Weighting	0.063	0.085
\mathcal{L}_{co} : Polar Coordinate \rightarrow Cartesian Coordinate	0.083	0.086
\mathcal{L}_{tg} : w/o Selection Mechanism	0.088	0.106
\mathcal{L}_{fc} : w/ Neighbor as Negative Sample	0.064	0.139
\mathcal{L}_{cm} : Acc. Consistency \rightarrow Vel. Consistency	0.066	0.068
Ours	0.053	0.053

TABLE IX

THE EFFECTS OF GAUSSIAN UPDATE AND REGULARIZATION STRATEGY.

Strategy	Geometric Quality			Rendering Quality		
	F-Score \uparrow	CD \downarrow	MHD \downarrow	PSNR \uparrow	SSIM \uparrow	LPIPS \downarrow
Baseline	0.401	1.063	0.583	17.546	0.525	0.547
+ Ground Completion	0.422	0.937	0.506	17.885	0.531	0.540
+ NB Pruning	0.465	0.898	0.377	18.064	0.538	0.535
+ GA Densification	0.511	0.837	0.270	18.565	0.542	0.527
+ Sky Decoupling	0.528	0.787	0.227	18.582	0.542	0.526
+ Depth & Normal Loss	0.542	0.750	0.186	18.738	0.549	0.513
+ Multi-view Constraint	0.558	0.725	0.159	19.406	0.562	0.492

their contributions and the rationality of our framework design.

1) *Self-supervised Signals*: In Tab. VII, we perform a series of experiments on the VoD with extremely sparse points. \mathcal{L}_{cd} and \mathcal{L}_{co} are cluster-based distance and column occupancy loss. \mathcal{L}_{tg} and \mathcal{L}_{ga} stand for teacher guidance and GMM alignment loss, while \mathcal{L}_{fc} and \mathcal{L}_{cm} represent feature-level and temporal constraints. At first, the use of \mathcal{L}_{co} leads to reduced odometry errors, especially in r_{rel} , as its larger-scale column comparison with occupancy representation is more sensitive to rotational discrepancies and can ease noise from point-to-point constraint \mathcal{L}_{cd} . Then, by incorporating soft labels derived from geometry-based pose refinement, \mathcal{L}_{tg} guides the network to predict more reasonable results and avoid getting stuck in local optima due to rigid geometric constraints. Using \mathcal{L}_{fc} further reduces t_{rel} and r_{rel} , validating that the discriminative features derived by contrastive learning of farthest and nearest points make model easier to identify inter-frame relationships. Besides, the results in the 5th, 6th and 7th rows demonstrate that the acceleration constraint \mathcal{L}_{cm} is crucial for suppressing abnormal poses, and that the cluster cues are critical for reducing feature correlation between unrelated instances.

2) *Self-supervised Strategy Selection*: We show the impact of various self-supervised strategies in Tab. VIII. The 1st row

TABLE X
THE EFFECTS OF VIEW COUNT ON MULTI-VIEW REGULARIZATION.

Number of views	F-Score \uparrow	CD \downarrow	MHD \downarrow	PSNR \uparrow	SSIM \uparrow	LPIPS \downarrow
Two	0.549	0.736	0.171	19.121	0.554	0.509
Three	0.553	0.729	0.166	19.291	0.559	0.499
Ours (Five)	0.558	0.725	0.159	19.406	0.562	0.492

TABLE XI
GEOMETRIC AND RENDERING QUALITY EVALUATION ON THE GARDEN SEQUENCE OF NTU4DRADLM BASED ON THERMAL IMAGES. * INDICATES NOT USING NORMAL CONSTRAINTS.

Method	F-Score \uparrow	CD \downarrow	MHD \downarrow	PSNR \uparrow	SSIM \uparrow	LPIPS \downarrow
GaussianPro	0.633	0.590	0.080	22.355	0.680	0.478
2DGS	0.295	0.830	0.224	18.456	0.634	0.556
3DGS	0.572	0.561	0.102	21.984	0.676	0.491
Ours*	0.666	0.445	0.058	25.875	0.715	0.436

shows that assigning higher weights to larger clusters is effective in \mathcal{L}_{cd} . Polar coordinates exhibit superiority over cartesian coordinates when transforming points into BEV for column comparison in \mathcal{L}_{co} . Besides, without a selection mechanism in \mathcal{L}_{tg} , suboptimal soft labels would misguide the model, causing performance degradation. Using the farthest point rather than the neighbor with similar features as a negative sample in \mathcal{L}_{fc} is more reasonable, as demonstrated in the 4th row. Finally, the constant velocity assumption adversely affects the network learning, due to frequent speed variations in real-world driving.

3) *Gaussian Update and Regularization*: We conduct ablation studies on the NTU4DRadLM dataset with various scenes to evaluate map optimization. As illustrated in Tab. IX, ground completion improves geometric quality because the radar map lacks ground structure initially. The improvement in ground rendering is also evident in 3rd and 4th rows of Fig. 12. Since neighborhood-based (NB) pruning preserves useful gaussians for splitting and geometry-aware (GA) densification produces more gaussians in structurally appropriate positions to complete voids, all metrics further achieve a consistent boost. The results in the 5th row of Tab. IX exhibit that the sky decoupling strategy improves map quality by using a sky mask to remove floaters. A qualitative example of this enhancement is shown in Fig. 15. The 6th row of Tab. IX and Fig. 16 demonstrate that geometric knowledge of visual fundamental models serves as effective constraints. Finally, we mitigate the spatial ambiguity of a single view through multi-view collaborative constraints in overlap regions, resulting in the best performance. In Tab. X, we further explore the effect of view count. The results prove that using constraints from more perspectives facilitates proper convergence of gaussian attributes, leading to better results.

E. Application Potential with Thermal Image

While RGB images are available in most environments, they degrade in low-light nights. In contrast, thermal images exhibit

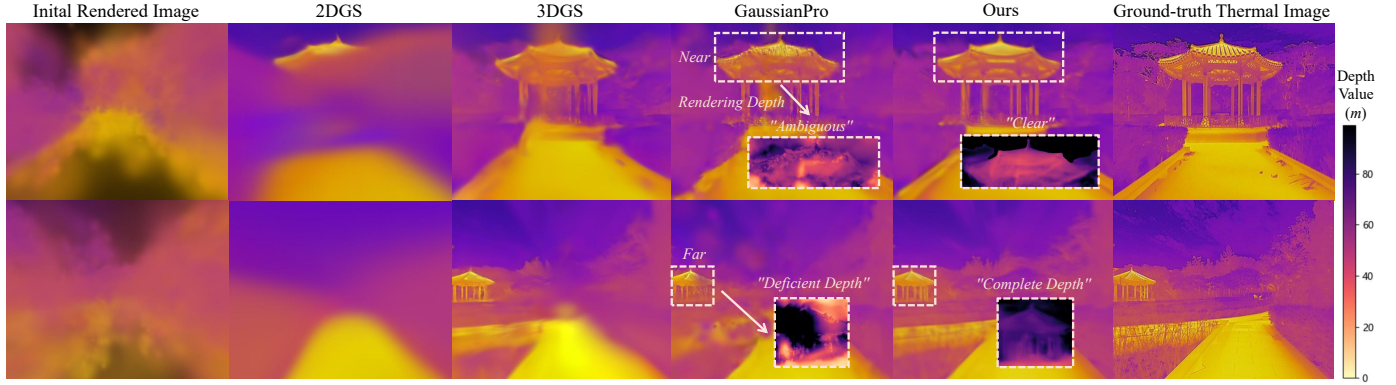


Fig. 17. Comparisons of thermal images rendered in the garden sequence of NTU4DRadLM. We highlight the rendered depth of nearby and distant objects.

TABLE XII
4D RADAR ODOMETRY EXPERIMENT RESULTS ON SELF-COLLECTED CAMPUS DATASET.

Method	Gym (300m)			Building2 (370m)			Straight (205m)			Parking2 (234m)			Mean		
	RPE(m)	RPE($^{\circ}$)	ATE(m)	RPE(m)	RPE($^{\circ}$)	ATE(m)	RPE(m)	RPE($^{\circ}$)	ATE(m)	RPE(m)	RPE($^{\circ}$)	ATE(m)	RPE(m)	RPE($^{\circ}$)	ATE(m)
ICP	0.886	1.913	7.677	0.903	2.149	10.330	1.414	2.612	13.945	0.770	1.939	5.595	0.993	2.153	9.387
NDT	<u>0.785</u>	3.715	<u>4.751</u>	2.161	8.463	24.089	5.617	32.763	26.836	2.046	9.028	20.961	2.652	13.492	19.159
GICP	3.337	5.031	26.357	3.721	6.532	22.384	5.754	10.316	16.307	3.983	5.893	16.490	4.199	6.943	20.384
APDGICP	1.608	2.914	11.619	2.196	3.932	17.340	5.049	6.047	29.351	2.359	3.082	12.517	2.803	3.994	17.707
RaFlow	5.623	9.010	50.921	5.012	10.804	48.504	5.112	<u>2.569</u>	46.497	4.666	13.803	32.208	5.103	9.047	44.533
Ours	0.440	1.878	2.316	0.477	1.778	7.166	0.542	1.913	4.882	0.626	<u>2.728</u>	2.663	0.521	2.074	4.257

TABLE XIII
THE PERFORMANCE OF MAP OPTIMIZATION AND IMAGE RENDERING ON SELF-COLLECTED CAMPUS DATASET.

Method	Gym			Building2			Straight			Parking2			Mean		
	F-Score \uparrow	CD \downarrow	MHD \downarrow	F-Score \uparrow	CD \downarrow	MHD \downarrow	F-Score \uparrow	CD \downarrow	MHD \downarrow	F-Score \uparrow	CD \downarrow	MHD \downarrow	F-Score \uparrow	CD \downarrow	MHD \downarrow
GaussianPro	<u>0.276</u>	5.973	0.673	0.230	5.733	1.164	0.297	2.290	0.366	0.349	4.902	0.678	<u>0.288</u>	4.724	0.720
2DGS	0.118	1.669	0.959	0.088	<u>1.835</u>	1.262	0.144	1.467	0.692	0.181	1.370	1.824	0.133	<u>1.585</u>	1.184
3DGS	0.267	<u>1.210</u>	<u>0.422</u>	0.198	3.531	<u>1.012</u>	0.298	<u>0.898</u>	0.319	0.389	0.938	<u>0.274</u>	<u>0.288</u>	1.644	<u>0.507</u>
Ours	0.341	0.974	0.377	0.283	1.577	0.586	0.362	0.818	0.328	0.484	0.854	0.173	0.367	1.056	0.366
	PSNR \uparrow	SSIM \uparrow	LPIPS \downarrow	PSNR \uparrow	SSIM \uparrow	LPIPS \downarrow	PSNR \uparrow	SSIM \uparrow	LPIPS \downarrow	PSNR \uparrow	SSIM \uparrow	LPIPS \downarrow	PSNR \uparrow	SSIM \uparrow	LPIPS \downarrow
GaussianPro	<u>20.081</u>	<u>0.584</u>	0.459	<u>20.970</u>	<u>0.671</u>	<u>0.437</u>	<u>19.461</u>	0.498	0.512	21.122	0.683	0.346	<u>20.408</u>	<u>0.609</u>	0.439
2DGS	18.535	0.566	0.548	17.127	0.606	0.532	18.695	0.491	0.600	19.093	0.647	0.487	18.362	0.577	0.542
3DGS	18.467	0.557	0.516	18.911	0.640	0.474	19.131	<u>0.509</u>	0.547	<u>21.141</u>	<u>0.705</u>	0.383	19.412	0.602	0.480
Ours	21.273	0.602	<u>0.468</u>	23.177	0.699	0.408	20.756	<u>0.524</u>	<u>0.519</u>	22.853	0.724	<u>0.366</u>	22.015	0.637	<u>0.440</u>

greater stability across diverse scenarios. To reveal the infrared potential and prove the adaptability of our method to different visual sensors, we adopt thermal images for map optimization in this part. As NTU4DRadLM does not provide thermal data for *Cp* and *Nyl* sequences, we evaluate solely on the *Garden* in Tab. XI, where our approach omits normal constraints owing to Metric3D’s [51] inability to estimate normals from thermal images. Nonetheless, the results indicate that our method still outperforms GaussianPro by 3.520 PSNR and achieves advantages across all metrics of geometric quality, demonstrating its generalization and prospects for radar-thermal reconstruction. In Fig. 17, we illustrate the infrared rendering results, and our framework can better restore the details of ground and building while getting reasonable depths for nearby and distant objects.

F. More Experiments on Self-collected Campus Dataset

To validate our method’s effectiveness in real-world scenarios beyond public datasets and in nighttime scene reconstruction not supported by NTU4DRadLM [9], we conduct extensive experiments based on our self-collected dataset acquired from a handheld platform, thereby providing a more thorough

validation of our algorithm alongside the results presented in Sec. V-C.

1) *4D Radar Odometry*: We present the evaluation results of our self-collected dataset in Tab. XII. It indicates that our method achieves state-of-the-art performance with translation and rotation RPEs of 0.521 and 2.074, respectively. In contrast to the results in Tab. IV, both APDGICP and GICP exhibit substantially inferior performance to ICP. We attribute this to the sparser points in our radar data compared to NTU4DRadLM, which significantly influences the effectiveness of GICP-based methods due to their dependence on distinct local structures. Furthermore, we show the trajectories of odometry in Fig. 18. As a result of unstable inter-frame registration caused by low-quality radar points, the paths of GICP-based methods display significant fluctuations. By comparison, benefiting from radar-specific designs, namely the cluster-aware matching for robust data association and multi-level constraints for reliable pose prediction, our method obtains smoother trajectories in Fig. 18. Meanwhile, by using a cluster-weighted point-to-point loss and enforcing large-scale consistency through column comparison, our proposed algorithm outperforms ICP in both quantitative metrics (4.257 vs. 9.387 ATE) and visual comparisons.

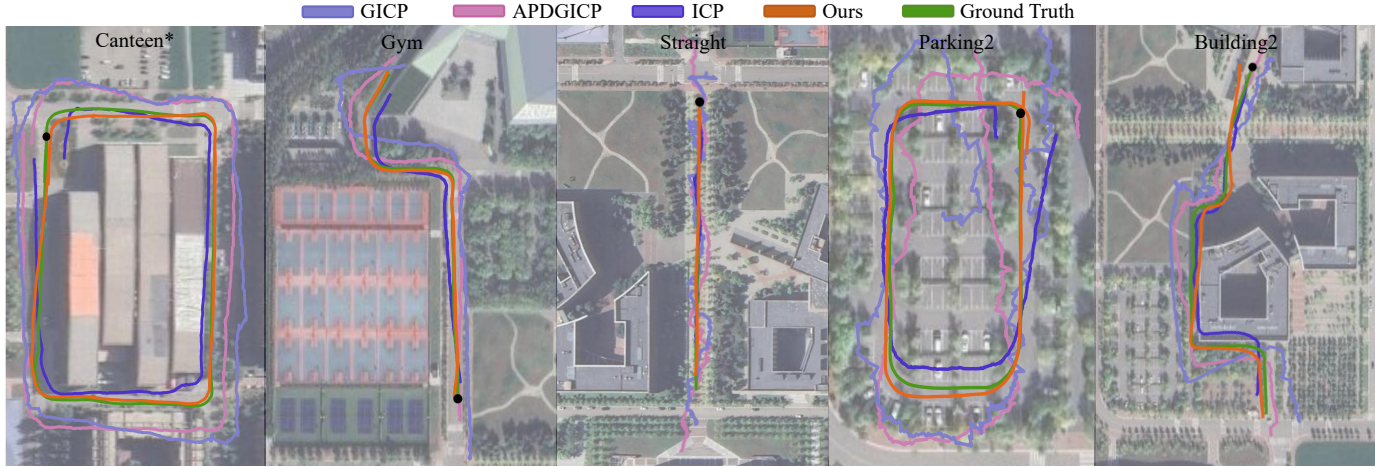


Fig. 18. Trajectory comparison of various methods using different colors on our self-collected campus dataset. * indicates the sequence from the training set.

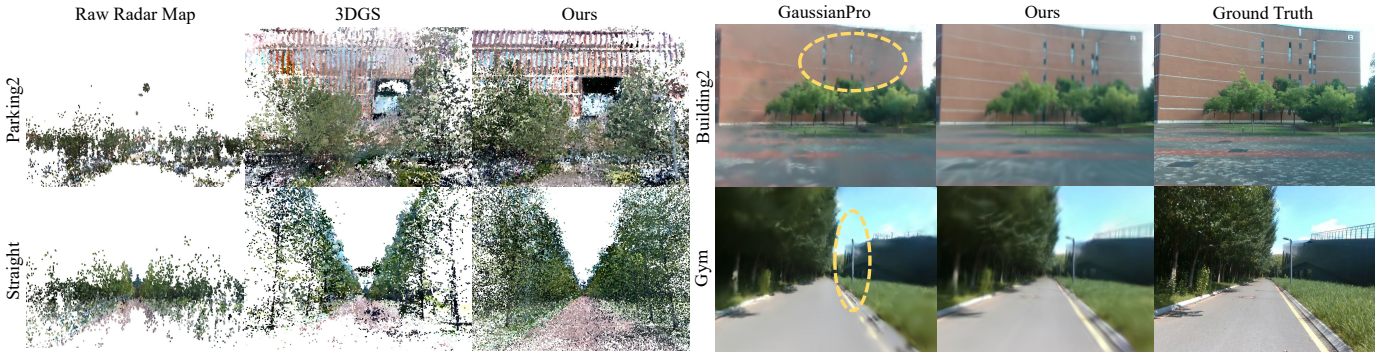


Fig. 19. Comparison of optimized radar maps and rendered images on self-collected dataset. Yellow circles mark the defective rendering areas in GaussianPro.

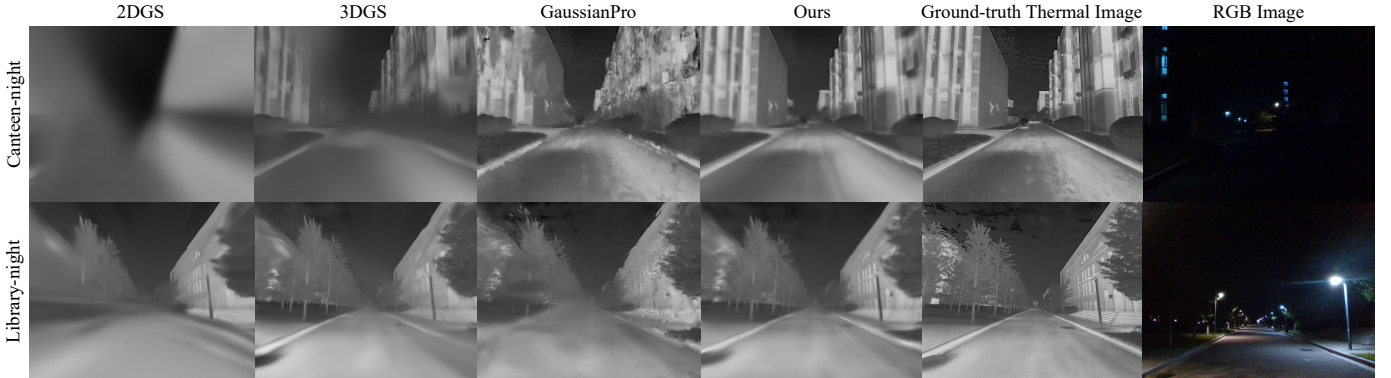


Fig. 20. Comparison of thermal images rendered from the night sequences of our self-collected dataset. We also display the corresponding RGB images.

TABLE XIV

MEAN GEOMETRIC AND RENDERING QUALITY OVER NIGHT SEQUENCES
IN THE SELF-COLLECTED DATASET BASED ON THERMAL IMAGES. *
INDICATES NOT USING NORMAL CONSTRAINTS.

Method	F-Score \uparrow	CD \downarrow	MHD \downarrow	PSNR \uparrow	SSIM \uparrow	LPIPS \downarrow
GaussianPro	0.171	5.052	4.965	23.650	0.756	0.418
2DGS	0.113	1.764	1.849	22.936	0.762	0.463
3DGS	0.232	1.613	1.111	23.026	0.765	0.433
Ours*	0.264	1.322	0.559	25.993	0.792	0.414

2) *Map Optimization*: In Tab. XIII, we present a comprehensive comparison of both geometric reconstruction accuracy and novel view rendering quality across different approaches. Results show that GaussianPro achieves competitive rendering quality but poorer geometric precision, with a chamfer distance (CD) three times greater than 3DGS. This may be caused by inaccurate propagation depth of the newly added gaussians. In

contrast, our algorithm achieves a better balance between the geometry and rendering quality, with a CD merely 64% that of 3DGS. For a more intuitive comparison, we further visualize the optimized local radar maps and rendered images in Fig. 19. Benefiting from ground completion and geometry-aware densification that generates new gaussians with reasonable spatial positions, our algorithm not only reconstructs maps with more complete and denser structures but also renders images with higher clarity.

3) *Radar-Thermal Reconstruction*: As the NTU4DRadLM contains only daytime sequences, we collect nighttime data for our campus dataset and conduct more experiments to explore the potential for radar-thermal reconstruction under low light. As displayed in Tab. XIV, our algorithm achieves an MHD of 0.559 for geometric quality, about half that of 3DGS, and surpasses GaussianPro by 2.343 in PSNR for image rendering.

We further visualize rendering results in Fig. 20, where our method also generates novel view thermal images with clearer details than other approaches, proving the effectiveness of the proposed modules across different image modalities.

VI. CONCLUSIONS

In this article, we introduce the first 4D radar-based framework, called *Super4DR*, which contains learning-based odometry estimation and map optimization while explicitly accounting for radar-specific characteristics. It can predict poses based on noisy and sparse radar points, reconstruct dense structures from low-quality radar maps, and render multi-modal images with depth and normal maps. *For odometry estimation*, we first propose a cluster-aware network, which leverages object-level cues to perform robust inter-frame matching and is trained by multi-level self-supervised losses for label-free learning. Under consideration of radar point distribution, cluster-weighted distance and column occupancy losses are adopted to constrain geometric consistency. A teacher guidance loss then uses soft labels as additional supervision to perform knowledge transfer. The feature contrast and temporal constraint are also applied to enable effective matching and improve trajectory smoothness. *For map optimization*, we propose a gaussian-based optimizer that views 3D gaussians as an intermediate map representation. It contains a depth-guided completion module for the ground recovery, combined with a radar-specific densification module aimed at improving map integrity. The selective separation and multi-view regularization are further used to decrease floaters, avoid mistaken deletion and accelerate optimization. Extensive experiments on public and self-collected datasets show that our method achieves superior results in various aspects, including odometry accuracy, map geometric quality and rendering detail fidelity. We further explore the potential of 4D radar-thermal reconstruction in poor illumination and verify the applicability of our method across different visual sensors.

REFERENCES

- [1] J. Zhang, H. Zhuge, Z. Wu, G. Peng, M. Wen, Y. Liu, and D. Wang, “4dradar slam: A 4d imaging radar slam system for large-scale environments based on pose graph optimization,” in *2023 IEEE International Conference on Robotics and Automation (ICRA)*, pp. 8333–8340, IEEE, 2023.
- [2] X. Wu, Y. Chen, Z. Li, Z. Hong, and L. Hu, “Efear-4d: Ego-velocity filtering for efficient and accurate 4d radar odometry,” *IEEE Robotics and Automation Letters*, vol. 9, no. 11, pp. 9828–9835, 2024.
- [3] D. C. Herraez, M. Zeller, L. Chang, I. Vizzo, M. Heidingsfeld, and C. Stachniss, “Radar-only odometry and mapping for autonomous vehicles,” in *2024 IEEE International Conference on Robotics and Automation (ICRA)*, pp. 10275–10282, 2024.
- [4] S. Kim, J. Seok, J. Lee, and K. Jo, “Radar4motion: Imu-free 4d radar odometry with robust dynamic filtering and rcs-weighted matching,” *IEEE Transactions on Intelligent Vehicles*, pp. 1–11, 2024.
- [5] S. Lu, G. Zhuo, L. Xiong, X. Zhu, L. Zheng, Z. He, M. Zhou, X. Lu, and J. Bai, “Efficient deep-learning 4d automotive radar odometry method,” *IEEE Transactions on Intelligent Vehicles*, 2023.
- [6] G. Zhuoins, S. Lu, L. Xiong, H. Zhouins, L. Zheng, and M. Zhou, “4drv-net: Deep 4d radar-visual odometry using multi-modal and multi-scale adaptive fusion,” *IEEE Transactions on Intelligent Vehicles*, 2023.
- [7] H. Zhou, S. Lu, and G. Zhuo, “Self-supervised 4-d radar odometry for autonomous vehicles,” in *2023 IEEE 26th International Conference on Intelligent Transportation Systems (ITSC)*, pp. 764–769, 2023.
- [8] F. Ding, Z. Pan, Y. Deng, J. Deng, and C. X. Lu, “Self-supervised scene flow estimation with 4-d automotive radar,” *IEEE Robotics and Automation Letters*, vol. 7, no. 3, pp. 8233–8240, 2022.
- [9] J. Zhang, H. Zhuge, Y. Liu, G. Peng, Z. Wu, H. Zhang, Q. Lyu, H. Li, C. Zhao, D. Kircali, *et al.*, “Ntu4dradlm: 4d radar-centric multi-modal dataset for localization and mapping,” in *2023 IEEE 26th International Conference on Intelligent Transportation Systems (ITSC)*, pp. 4291–4296, IEEE, 2023.
- [10] R. Zhang, D. Xue, Y. Wang, R. Geng, and F. Gao, “Towards dense and accurate radar perception via efficient cross-modal diffusion model,” *IEEE Robotics and Automation Letters*, vol. 9, no. 9, pp. 7429–7436, 2024.
- [11] K. Luan, C. Shi, N. Wang, Y. Cheng, H. Lu, and X. Chen, “Diffusion-based point cloud super-resolution for mmwave radar data,” in *2024 IEEE International Conference on Robotics and Automation (ICRA)*, pp. 11171–11177, 2024.
- [12] B. Kerbl, G. Kopanas, T. Leimkühler, and G. Drettakis, “3d gaussian splatting for real-time radiance field rendering,” *ACM Trans. Graph.*, vol. 42, no. 4, pp. 139–1, 2023.
- [13] P. J. Besl and N. D. McKay, “Method for registration of 3-d shapes,” in *Sensor fusion IV: control paradigms and data structures*, vol. 1611, pp. 586–606, Spie, 1992.
- [14] A. Segal, D. Haehnel, and S. Thrun, “Generalized-icp,” in *Robotics: science and systems*, vol. 2, p. 435, Seattle, WA, 2009.
- [15] I. Vizzo, T. Guadagnino, B. Mersch, L. Wiesmann, J. Behley, and C. Stachniss, “Kiss-icp: In defense of point-to-point icp-simple, accurate, and robust registration if done the right way,” *IEEE Robotics and Automation Letters*, vol. 8, no. 2, pp. 1029–1036, 2023.
- [16] P. Biber and W. Straßer, “The normal distributions transform: A new approach to laser scan matching,” in *Proceedings 2003 IEEE/RSJ International Conference on Intelligent Robots and Systems (IROS 2003)(Cat. No. 03CH37453)*, vol. 3, pp. 2743–2748, IEEE, 2003.
- [17] J. Zhang, S. Singh, *et al.*, “Loam: Lidar odometry and mapping in real-time.,” in *Robotics: Science and systems*, vol. 2, pp. 1–9, Berkeley, CA, 2014.
- [18] T. Shan and B. Englot, “Lego-loam: Lightweight and ground-optimized lidar odometry and mapping on variable terrain,” in *2018 IEEE/RSJ International Conference on Intelligent Robots and Systems (IROS)*, pp. 4758–4765, IEEE, 2018.
- [19] H. Wang, C. Wang, C.-L. Chen, and L. Xie, “F-loam: Fast lidar odometry and mapping,” in *2021 IEEE/RSJ International Conference on Intelligent Robots and Systems (IROS)*, pp. 4390–4396, IEEE, 2021.
- [20] G. Wang, X. Wu, Z. Liu, and H. Wang, “Pwclo-net: Deep lidar odometry in 3d point clouds using hierarchical embedding mask optimization,” in *Proceedings of the IEEE/CVF conference on computer vision and pattern recognition*, pp. 15910–15919, 2021.
- [21] G. Wang, X. Wu, S. Jiang, Z. Liu, and H. Wang, “Efficient 3d deep lidar odometry,” *IEEE Transactions on Pattern Analysis and Machine Intelligence*, vol. 45, no. 5, pp. 5749–5765, 2023.
- [22] J. Liu, G. Wang, C. Jiang, Z. Liu, and H. Wang, “Translo: A window-based masked point transformer framework for large-scale lidar odometry,” in *Proceedings of the AAAI Conference on Artificial Intelligence*, vol. 37, pp. 1683–1691, 2023.
- [23] H. Zhang, G. Wang, X. Wu, C. Xu, M. Ding, M. Tomizuka, W. Zhan, and H. Wang, “Dslo: Deep sequence lidar odometry based on inconsistent spatio-temporal propagation,” in *2024 IEEE/RSJ International Conference on Intelligent Robots and Systems (IROS)*, pp. 10672–10677, 2024.
- [24] J. Nubert, S. Khattak, and M. Hutter, “Self-supervised learning of lidar odometry for robotic applications,” in *2021 IEEE International Conference on Robotics and Automation (ICRA)*, pp. 9601–9607, 2021.
- [25] B. Zhou, Y. Tu, Z. Jin, C. Xu, and H. Kong, “Hpplo-net: Unsupervised lidar odometry using a hierarchical point-to-plane solver,” *IEEE Transactions on Intelligent Vehicles*, vol. 9, no. 1, pp. 2727–2739, 2024.
- [26] Y. Xu, J. Lin, J. Shi, G. Zhang, X. Wang, and H. Li, “Robust self-supervised lidar odometry via representative structure discovery and 3d inherent error modeling,” *IEEE Robotics and Automation Letters*, vol. 7, no. 2, pp. 1651–1658, 2022.
- [27] D. Adolfsson, M. Magnusson, A. Alhashimi, A. J. Lilienthal, and H. Andreasson, “Cfear radarodometry - conservative filtering for efficient and accurate radar odometry,” in *2021 IEEE/RSJ International Conference on Intelligent Robots and Systems (IROS)*, pp. 5462–5469, 2021.
- [28] H. Lim, K. Han, G. Shin, G. Kim, S. Hong, and H. Myung, “Orora: Outlier-robust radar odometry,” in *2023 IEEE International Conference on Robotics and Automation (ICRA)*, pp. 2046–2053, 2023.
- [29] R. Zhang, Y. Zhang, D. Fu, and K. Liu, “Scan denoising and normal distribution transform for accurate radar odometry and positioning,”

IEEE Robotics and Automation Letters, vol. 8, no. 3, pp. 1199–1206, 2023.

[30] F. Ding, A. Palfy, D. M. Gavrila, and C. X. Lu, “Hidden gems: 4d radar scene flow learning using cross-modal supervision,” in *Proceedings of the IEEE/CVF Conference on Computer Vision and Pattern Recognition*, pp. 9340–9349, 2023.

[31] Z. Li, Y. Cui, N. Huang, C. Pang, and Z. Fang, “Cao-ronet: A robust 4d radar odometry with exploring more information from low-quality points,” *arXiv preprint arXiv:2503.01438*, 2025.

[32] B. Mildenhall, P. P. Srinivasan, M. Tancik, J. T. Barron, R. Ramamoorthi, and R. Ng, “Nerf: Representing scenes as neural radiance fields for view synthesis,” *Communications of the ACM*, vol. 65, no. 1, pp. 99–106, 2021.

[33] K. Cheng, X. Long, K. Yang, Y. Yao, W. Yin, Y. Ma, W. Wang, and X. Chen, “Gaussianpro: 3d gaussian splatting with progressive propagation,” in *Forty-first International Conference on Machine Learning*, 2024.

[34] J. Li, J. Zhang, X. Bai, J. Zheng, X. Ning, J. Zhou, and L. Gu, “Dngaussian: Optimizing sparse-view 3d gaussian radiance fields with global-local depth normalization,” in *Proceedings of the IEEE/CVF conference on computer vision and pattern recognition*, pp. 20775–20785, 2024.

[35] B. Huang, Z. Yu, A. Chen, A. Geiger, and S. Gao, “2d gaussian splatting for geometrically accurate radiance fields,” in *ACM SIGGRAPH 2024 conference papers*, pp. 1–11, 2024.

[36] R. Xiao, W. Liu, Y. Chen, and L. Hu, “Liv-gs: Lidar-vision integration for 3d gaussian splatting slam in outdoor environments,” *IEEE Robotics and Automation Letters*, vol. 10, no. 1, pp. 421–428, 2025.

[37] K. Wu, K. Zhang, Z. Zhang, M. Tie, S. Yuan, J. Zhao, Z. Gan, and W. Ding, “Hgs-mapping: Online dense mapping using hybrid gaussian representation in urban scenes,” *IEEE Robotics and Automation Letters*, vol. 9, no. 11, pp. 9573–9580, 2024.

[38] X. Zhou, Z. Lin, X. Shan, Y. Wang, D. Sun, and M.-H. Yang, “Drivinggaussian: Composite gaussian splatting for surrounding dynamic autonomous driving scenes,” in *Proceedings of the IEEE/CVF conference on computer vision and pattern recognition*, pp. 21634–21643, 2024.

[39] X. Liu, Z. Liu, F. Kong, and F. Zhang, “Large-scale lidar consistent mapping using hierarchical lidar bundle adjustment,” *IEEE Robotics and Automation Letters*, vol. 8, no. 3, pp. 1523–1530, 2023.

[40] C. Pang, Z. Shen, R. Yuan, C. Xu, and Z. Fang, “Lm-mapping: Large-scale and multi-session point cloud consistent mapping,” *IEEE Robotics and Automation Letters*, vol. 9, no. 12, pp. 10866–10873, 2024.

[41] M. Ester, H.-P. Kriegel, J. Sander, and X. Xu, “Density-based spatial clustering of applications with noise,” in *Int. Conf. knowledge discovery and data mining*, vol. 240, 1996.

[42] X. Liu, C. R. Qi, and L. J. Guibas, “Flownet3d: Learning scene flow in 3d point clouds,” in *Proceedings of the IEEE/CVF conference on computer vision and pattern recognition*, pp. 529–537, 2019.

[43] W. Wu, Z. Y. Wang, Z. Li, W. Liu, and L. Fuxin, “Pointpwc-net: Cost volume on point clouds for (self-) supervised scene flow estimation,” in *Computer Vision–ECCV 2020: 16th European Conference, Glasgow, UK, August 23–28, 2020, Proceedings, Part V 16*, pp. 88–107, Springer, 2020.

[44] K. Cho, B. Van Merriënboer, C. Gulcehre, D. Bahdanau, F. Bougares, H. Schwenk, and Y. Bengio, “Learning phrase representations using rnn encoder-decoder for statistical machine translation,” *arXiv preprint arXiv:1406.1078*, 2014.

[45] G. Hinton, O. Vinyals, and J. Dean, “Distilling the knowledge in a neural network,” *arXiv preprint arXiv:1503.02531*, 2015.

[46] A. Mishra and D. Marr, “Apprentice: Using knowledge distillation techniques to improve low-precision network accuracy,” *arXiv preprint arXiv:1711.05852*, 2017.

[47] Z. Fang, J. Wang, L. Wang, L. Zhang, Y. Yang, and Z. Liu, “Seed: Self-supervised distillation for visual representation,” *arXiv preprint arXiv:2101.04731*, 2021.

[48] P. He, P. Emami, S. Ranka, and A. Rangarajan, “Self-supervised robust scene flow estimation via the alignment of probability density functions,” in *Proceedings of the AAAI Conference on Artificial Intelligence*, vol. 36, pp. 861–869, 2022.

[49] L. Yang, B. Kang, Z. Huang, Z. Zhao, X. Xu, J. Feng, and H. Zhao, “Depth anything v2,” *Advances in Neural Information Processing Systems*, vol. 37, pp. 21875–21911, 2024.

[50] B. Cheng, I. Misra, A. G. Schwing, A. Kirillov, and R. Girdhar, “Masked-attention mask transformer for universal image segmentation,” in *Proceedings of the IEEE/CVF conference on computer vision and pattern recognition*, pp. 1290–1299, 2022.

[51] M. Hu, W. Yin, C. Zhang, Z. Cai, X. Long, H. Chen, K. Wang, G. Yu, C. Shen, and S. Shen, “Metric3d v2: A versatile monocular geometric foundation model for zero-shot metric depth and surface normal estimation,” *IEEE Transactions on Pattern Analysis and Machine Intelligence*, vol. 46, no. 12, pp. 10579–10596, 2024.

[52] A. Palfy, E. Pool, S. Baratam, J. F. Kooij, and D. M. Gavrila, “Multi-class road user detection with 3+ 1d radar in the view-of-delft dataset,” *IEEE Robotics and Automation Letters*, vol. 7, no. 2, pp. 4961–4968, 2022.

[53] W. Xu and F. Zhang, “Fast-llo: A fast, robust lidar-inertial odometry package by tightly-coupled iterated kalman filter,” *IEEE Robotics and Automation Letters*, vol. 6, no. 2, pp. 3317–3324, 2021.

[54] Q. Li, S. Chen, C. Wang, X. Li, C. Wen, M. Cheng, and J. Li, “Lonet: Deep real-time lidar odometry,” in *Proceedings of the IEEE/CVF Conference on Computer Vision and Pattern Recognition*, pp. 8473–8482, 2019.

[55] S. Lu, H. Zhou, and G. Zhuo, “Dnoi-4dro: Deep 4d radar odometry with differentiable neural-optimization iterations,” *arXiv preprint arXiv:2505.12310*, 2025.